Exploring compact binary merger host galaxies and environments with `zELDA`

S. Mandhai [1,2]⋆ G. P. Lamb,[1]⋆ N. R. Tanvir,[1]⋆ J. Bray,[3,4] C. J. Nixon [1], R. A. J. Eyles-Ferris,[1] A. J. Levan[5,6] and B. P. Gompertz [7]

[1]*School of Physics and Astronomy, University of Leicester, University Road, Leicester LE1 7RH, UK*
[2]*Jodrell Bank Centre for Astrophysics, Department of Physics and Astronomy, The University of Manchester, Manchester M13 9PY, UK*
[3]*Department of Physical Sciences, Robert Hooke Building, Kents Hill, Milton Keynes MK7 6AA, UK*
[4]*Department of Physics, The University of Auckland, Private Bag 92019, Auckland, New Zealand*
[5]*Department of Astrophysics/IMAPP, Radboud University, 6525 AJ Nijmegen, the Netherlands*
[6]*Department of Physics, University of Warwick, Coventry CV4 7AL, UK*
[7]*School of Physics and Astronomy, University of Birmingham, Birmingham B15 2TT, UK*

ABSTRACT

Compact binaries such as double neutron stars or a neutron star paired with a black hole, are strong sources of gravitational waves during coalescence and also the likely progenitors of various electromagnetic phenomena, notably short-duration gamma-ray bursts (SGRBs), and kilonovae. In this work, we generate populations of synthetic binaries and place them in galaxies from the large-scale hydrodynamical galaxy evolution simulation, EAGLE. With our zELDA code, binaries are seeded in proportion to star formation rate, and we follow their evolution to merger using both the BPASS and COSMIC binary stellar evolution codes. We track their dynamical evolution within their host galaxy potential, to estimate the galactocentric distance at the time of the merger. Finally, we apply observational selection criteria to allow comparison of this model population with the legacy sample of SGRBs. We find a reasonable agreement with the redshift distribution (peaking at $0.5 < z < 1$), host morphologies, and projected galactocentric offsets (modal impact parameter $\lesssim 10$ kpc). Depending on the binary simulation used, we predict ~ 16–35 per cent of SGRB events would appear 'host-less', i.e. sources that merge with high impact parameters or have hosts fainter than the detection limit ($H > 26$).

Key words: transients: gamma-ray bursts – transients: neutron star mergers – transient: black hole - neutron star mergers – galaxies: general – stars: kinematics and dynamics – binaries: close.

1 INTRODUCTION

The orbits of compact binaries (containing neutron stars or stellar mass black holes) decay via gravitational wave emission, with inspiral times ranging from a few Myr to many Hubble times. The final mergers have become of increasing interest following the first gravitational wave (GW) detections (Abbott et al. 2016). Where one or both of the components are a neutron star, such a coalescence can also produce detectable electromagnetic counterparts, opening the route to multimessenger astrophysics (Branchesi 2016; Abbott et al. 2017b; Huerta et al. 2019; Mészáros et al. 2019; Murase & Bartos 2019). This was exemplified by the historic discovery of GW170817, and the accompanying emission from both a kilonova and relativistic jetted material (Abbott et al. 2017c; Alexander et al. 2017; Arcavi et al. 2017; Chornock et al. 2017; Coulter et al. 2017; Cowperthwaite et al. 2017; Evans et al. 2017; Haggard et al. 2017; Hallinan et al. 2017; Im et al. 2017; Kasliwal et al. 2017; Levan et al. 2017; Margutti et al. 2017; McCully et al. 2017; Nicholl et al. 2017; Pian et al. 2017;

Shappee et al. 2017; Smartt et al. 2017; Soares-Santos et al. 2017; Tanaka et al. 2017; Tanvir et al. 2017; Troja et al. 2017; Villar et al. 2017; Corsi et al. 2018; Lyman et al. 2018; Mooley et al. 2018; Nynka et al. 2018; Resmi et al. 2018; Hajela et al. 2019; Lamb et al. 2019a; Piro et al. 2019; Troja et al. 2019a, 2020).

The kilonova is powered by the radioactive decay of newly synthesized heavy elements from ejected neutron star material, and may be the dominant site of r-process nucleosynthesis in our Universe. The kilonova accompanying GW170817 (AT2017gfo) was extensively studied from ultraviolet to infrared wavelengths, thanks to its relative proximity at ≈ 40 Mpc (Abbott et al. 2017c). However, more typically, the current generation of GW detectors[1,2] finds neutron–star containing mergers at ~ 200 Mpc (Abbott et al. 2018), which combined with the large (10s or 100s of sq. deg.) error regions, presents a significant challenge to counterpart searches (Mandhai et al. 2018; Dichiara et al. 2020).

The production of relativistic jets during mergers is less well understood, but is believed to be responsible for the short-duration gamma-

---

⋆ E-mail: soheb.mandhai@manchester.ac.uk (SM); gpl6@le.ac.uk (GPL); nrt3@le.ac.uk (NRT)

[1]Third Observing Run (O3).
[2]https://gracedb.ligo.org/superevents/public/O3/

ray burst (SGRB) emission; these events have typical durations, $T_{90} < 2\,\mathrm{s}$ (Mazets & Goolenetskii 1981; Kouveliotou et al. 1993). This emission is much brighter and can be seen at cosmological distances, indeed, apart from GRB 170817A accompanying GW170817, the nearest SGRB with a secure redshift is GRB 080905A at $z = 0.1218$ (Rowlinson et al. 2010) whilst the most distant SGRBs have been found at $z \gtrsim 2$ (e.g. Levan et al. 2006; Fong et al. 2017; Selsing et al. 2018). The association of SGRBs with compact binary mergers confirmed both by analysis of the non-thermal emission from AT2017gfo (Perego, Radice & Bernuzzi 2017; Wang et al. 2017), and the evidence of kilonova emission following other SGRBs (e.g. Tanvir et al. 2013; Jin et al. 2016; Gompertz et al. 2018; Lamb et al. 2019b; Troja et al. 2019b; Jin et al. 2020).

SGRBs were first localized to arcsec precision in the *Neil Gehrels Swift Observatory* (hereafter *Swift*) era, which resulted in the identifications of host galaxies and hence redshifts (e.g. Fox et al. 2005; Gehrels et al. 2005; Hjorth et al. 2005; Bloom et al. 2006). The typical redshifts for SGRBs at the depth reached by *Swift*/BAT is $z < 1$ (Lien et al. 2016). These events originate from a wide range of host galaxies and environments, including some with little or no ongoing star formation (e.g. Fong et al. 2013; Fong & Berger 2013; Berger 2014). The *Swift* rate of SGRB discovery is $\sim 10\,\mathrm{yr}^{-1}$, in contrast, detectors with larger fields of view such as the *Fermi*/GBM (Gamma-ray Burst Monitor) have a rate of $\sim 40\,\mathrm{yr}^{-1}$, although the *Fermi* localizations are much worse (typically an $\sim$ few $\times\,10\,\mathrm{deg}^2$), so redshifts are rarely obtained. Since the afterglows of SGRBs are also typically fainter than those from long-GRBs ($T_{90} > 2\,\mathrm{s}$), the net result is that the total sample of SGRBs with better constrained ($\sim$arcsec–arcmin) sky-positions is ~ 140, and only 25–30 per cent of these have confident redshifts (e.g. Fong et al. 2015a; Lien et al. 2016). It is worth cautioning that the assignation of a given GRB to the short-hard class is also uncertain in some cases (Bromberg et al. 2013), and also that a small proportion of the candidate host galaxies may be chance alignments rather than the real host (Levan et al. 2007). The existing sample should be understood to be incomplete and inhomogeneous, but still sufficient to show general trends.

Based on this observed population of SGRBs, a non-negligible fraction (~ 15 per cent; Fong et al. 2013) appear to have no obvious host galaxy. These events are considered 'host-less' and are typically seen at distances 30–75 kpc in projection from the nearest host galaxy candidate (Berger 2010; Fong & Berger 2013; Tunnicliffe et al. 2014). Studying the orbital evolution of the progenitor binary pairs relative to their host galaxy, before they merge, may allow us to investigate the frequency of progenitors migrating to distances such that they are classed host-less. Establishing constraints on the expected projected offsets of SGRBs, and the fraction of host-less events, may also aid in the efforts to identify the original host of the progenitor binary where it is uncertain, and by extension an improved understanding of the distribution of these compact binary mergers over the cosmological history. This combination of properties supports the compact binary merger hypothesis, in which the binary systems can have long lifetimes before merger, and can receive large kicks during the supernovae in which the compact remnants were formed (Hobbs et al. 2005; Nakar 2007).

In order to understand the relationship between the offsets of detected SGRBs and their host galaxies, we created a population of synthetic binaries and evolved them within hydrodynamically simulated galaxies. The compact binaries of interest discussed in this paper are primarily NSNS and BHNS as these are the most likely progenitors of SGRBs (Narayan, Paczynski & Piran 1992; Katz & Canel 1996; Narayan, Piran & Kumar 2001; Lee & Ramirez-Ruiz 2007). Previous studies have also explored the relationship between galaxies and the offsets of GRBs within static potentials

(e.g. Bloom, Sigurdsson & Pols 1999; Bulik, Belczyński & Zbijewski 1999; Bloom, Kulkarni & Djorgovski 2002; Belczynski et al. 2006; Church et al. 2011). In this study, we use updated stellar evolution prescriptions and evolving galaxy potentials to contrast with and predict observational SGRB offsets. The search for host galaxies and EM counterparts to GW events can be challenging as seen with the follow up of GW190814 (Ackley et al. 2020; Andreoni et al. 2020; Morgan et al. 2020). Studies such as the aforementioned and the one detailed in this paper are beneficial in improving the efficiency of follow-up campaigns by enabling prediction of the most likely host populations and offsets. We also comment on the merger rates predicted by our analysis, scaled by LIGO/VIRGO gravitational wave constraints for NSNS systems.

In this work, Section 2 introduces our code, ZELDA, that is used for the majority of the data analysis; in Section 3, we outline the results; in Section 4, we compare our results with observations of SGRBs; in Section 5, we discuss the relationship of the host galaxies and SGRB localizations; and finally, in Section 6, we summarize our key findings.

2 ZELDA: REDSHIFT ELECTROMAGNETIC LOCALIZATION AND DEDUCTION ALGORITHM

The Redshift Electromagnetic Localization and Deduction Algorithm (ZELDA)[3] is a collection of scripts designed to process and evolve a population of compact binaries within synthetic galaxies. An overview of the ZELDA code schematic is shown in Fig. 1.[4] The objective of ZELDA is to determine the orbital and stellar evolution of binaries relative to their host galaxy environment.

Throughout, we have adopted the same flat ($k = 0$), Λ Friedmann cosmology as used for the EAGLE simulation. Specifically, the density parameters for matter and dark energy are $\Omega_{M0} = 0.307$ and $\Omega_{\Lambda 0} = 0.693$, respectively, and the value for the Hubble constant used is $H_0 = 67.77\,\mathrm{km\ s}^{-1}\,\mathrm{Mpc}^{-1}$ (Planck Collaboration XVI 2014; Furlong et al. 2015).

2.1 Compact binaries

2.1.1 Formation channels

The evolution of binary stars with masses $> 8\,\mathrm{M}_\odot$ may result in the formation of compact binary systems that consist of a neutron star or a black hole paired with a neutron star, i.e. neutron star–neutron star (NSNS), or black hole-neutron star (BHNS).

For this study, we have simulated a population of synthetic compact binaries that are formed from the end-point evolution of regular, isolated, stellar binary systems. Compact binaries may also form through dynamical channels (e.g. Rodriguez et al. 2015; Rodriguez, Chatterjee & Rasio 2016; Fragione & Kocsis 2018; Rodriguez & Loeb 2018; Samsing & D'Orazio 2018; Andrews & Mandel 2019; Choksi et al. 2019; Fernández & Kobayashi 2019), for example in globular or nuclear clusters, or during galactic mergers (Palmese et al. 2017), although the merger rate of such binaries has been estimated to be small when compared to isolated binaries (Belczynski et al. 2018; Ye et al. 2019).

Recently Santoliquido et al. (2020) have argued that compact binaries formed in young stellar clusters will have a more significant contribution to global merger rates, increasing the rate of NSNS

---

[3]Repository: https://github.com/hirizon/zELDA-COMBIN
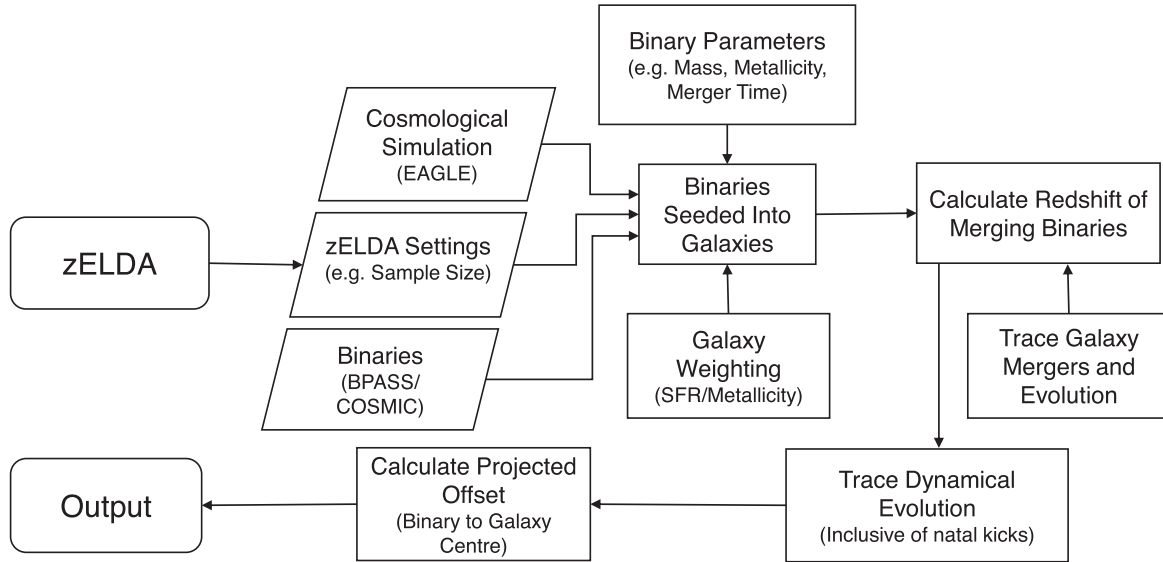[4]COSMOLOPY: http://roban.github.io/CosmoloPy/

Figure 1. A schematic breakdown of the PYTHON based ZELDA coding suite used within this study. Package dependencies include: NUMPY (Oliphant 2006), MATPLOTLIB (Hunter 2007), SCIPY (Virtanen et al. 2020), COSMOLOPY, PANDAS (McKinney 2010), ASTROPY (Astropy Collaboration 2013; Price-Whelan et al. 2018), and GALPY (Bovy 2015).

mergers by ∼50 per cent compared to isolated binaries alone. However, this conclusion also depends on their assumption of typically low natal-kicks for neutron stars, which itself seems inconsistent with the frequent large impact parameters seen for SGRBs. Therefore, we do not explicitly include dynamically formed systems within our calculations.

2.1.2 Simulated binary samples

Separate simulations were performed using two independent stellar evolution and population synthesis codes. For the first case, the binaries were produced by the Binary Population and Spectral Synthesis (BPASS v2.1 Eldridge et al. 2017) code[5] and processed through the Remnant Ejecta and Progenitor Explosion Relationship (REAPER) population synthesis code (Bray & Eldridge 2016). We use two configurations of compact remnant binaries from BPASS which correspond to the prescriptions highlighted in Bray & Eldridge (2018). Henceforth, these are referred to as BPASS/Bray[6] and BPASS/Hobbs, respectively. In short, both configurations use the detailed BPASS stellar evolution models; however, the net systematic kick velocities for each compact object in BPASS/Bray are calculated from a kick prescription based on the mass ratio of the supernova ejecta mass and the final mass of the compact object remnant while for the BPASS/Hobbs data set, the kick was randomly selected from the Maxwell–Boltzmann distribution outlined in Hobbs et al. (2005). In each case, the kicks are applied in random directions relative to the orbital plane of the binaries. The relative number of compact binaries that are non-disrupted is dependent on the kick prescription used.

The third set of simulated binaries were produced using the COSMIC v3.2.0/BSE code (Hurley, Tout & Pols 2002; Breivik et al. 2020). Binaries produced with BPASS are formed using detailed stellar

evolution models and prescriptions, whilst COSMIC uses analytical scalings and is best suited for rapid-population synthesis of binaries. Including binaries from COSMIC in our analysis allows us to more densely populate the parameter space, and reduce simulation noise by increasing the number of models sampled over, in comparison to the BPASS binaries used. Use of several codes to describe the stellar and binary evolution also allows us to compare and contrast results stemming from varied approaches. The net kick velocities for the COSMIC compact objects are obtained from a Maxwellian distribution with a velocity dispersion of $265 \, \mathrm{km \, s^{-1}}$ which is reduced by the factor of $1 - f_{\mathrm{fb}}$, where f_{fb} is the fraction of supernova ejecta falling back on to the remnant object (Fryer et al. 2012).

The stellar evolution codes provide outputs for a range of discrete metallicities. We use binaries corresponding to a sub-solar, metal poor ($Z = 0.004$) stellar population, a moderately metal abundant ($Z = 0.008$) population, and a roughly solar, metal rich ($Z = 0.02$) population. The role of metallicity in the formation of the binaries is discussed in Section 2.3.1. Noticeably, the COSMIC binaries exhibit lower merger times than the BPASS systems likely owing to the smaller separations between the compact objects within the sample. This can be cumulatively attributed to the differences in the adopted stellar evolutionary prescriptions between both simulations. COSMIC binaries initially have elliptical orbits and incorporate fallback on to the compact objects from ejected supernova material. Conversely for BPASS, the orbits of the binaries are circular and the supernova ejecta fallback is not considered. Other differences in simulation input fractions are also present and are detailed in Stanway & Eldridge (BPASS 2018) and Breivik et al. (COSMIC 2020). Within the work presented in this paper, BPASS/Bray is used as a primary fiducial model.

Whilst we expect the majority of NSNS binaries to produce an EM counterpart such as an SGRB, only BHNS systems with a comparatively small mass ratio are expected to. The formation of an EM counterpart depends on the ejecta mass released from the neutron star when merging with its companion black hole (Tanaka et al. 2014; Kawaguchi et al. 2016; Foucart et al. 2019; Hinderer et al. 2019). For more massive black holes the NS can pass the event horizon before it is tidally disrupted, therefore, stifling the

---

[5]Whilst BPASS v2.2 is available (Stanway & Eldridge 2018), we use an older version for consistency with the REAPER code.
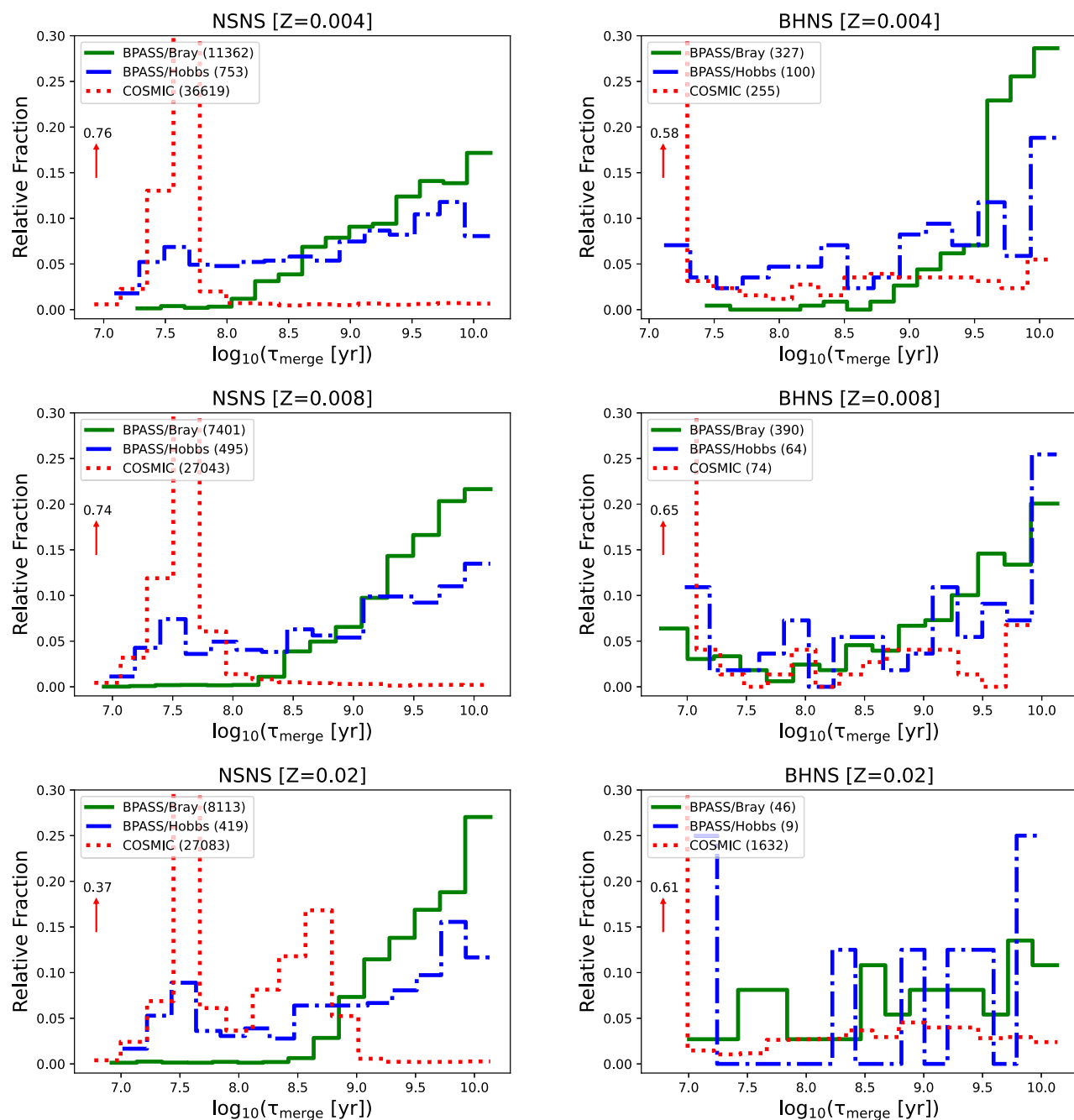[6]The demonstrative binary sample used for the figures and numerical values in the main text.

Figure 2. The normalized (by population) merger time distributions (i.e. N_{bin}/N_{tot}) for the seeded NSNS and eBHNS type binaries produced using different binary population synthesis configurations/packages. The top, middle, and bottom panels correspond to binaries with metallicities of $Z = 0.004$, 0.008, and 0.02, respectively. The numbers in brackets correspond to the total number of EM-bright unique models that are used for the binary seeding. We note an increase in systematic noise resulting from the relative rarity of eBHNS systems within the binary simulations used.

formation of an EM counterpart. The mass ratio of the black hole to neutron star, $Q = M_{BH}/M_{NS}$ is, therefore, crucial in governing the mass remaining following the coalescence of the binary (Shibata & Taniguchi 2011; Ruiz et al. 2020). However, a higher black hole spin increases the value of Q for which significant NS ejecta is expected (Barbieri et al. 2019). For this study, we use a $Q < 3$ threshold for the mass ratio (Hayashi et al. 2021). The notation of 'eBHNS' within this work refers to the potentially EM bright sub-population of systems that satisfy our condition. This applies to ~ 30–37 per cent and $\lesssim$ 1 per cent of the BPASS and COSMIC BHNS

binaries, respectively. Notably, COSMIC imposes a mass-gap between 3 and $5\,M_\odot$ which results in a smaller fraction of BHNS binaries within the Q threshold. The formation of these systems relative to the total BHNS population is rare. The number of unique eBHNS models produced by BPASS and COSMIC are relatively smaller than the simulated NSNS binaries. Regardless, we have included these binaries to account for their contribution towards the formation of SGRBs, although it does lead to a more sparse sampling of the merger time and kick velocity distributions for eBHNS systems, as is evident in Figs 2 and 3.
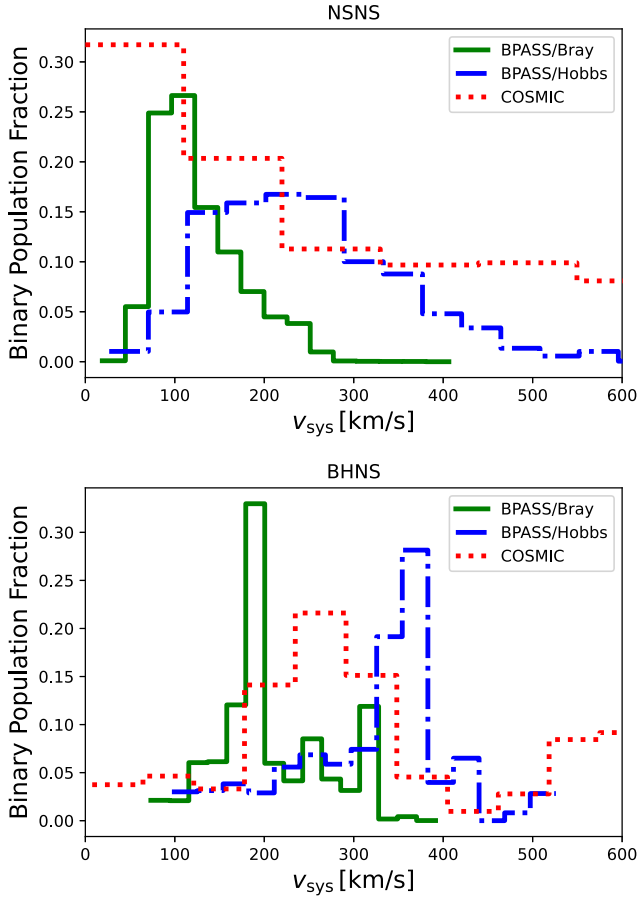
Figure 3. The final systematic velocity distributions corresponding to the seeded NSNS [upper] and eBHNS [lower] binaries for each simulation used.

2.2 Cosmological simulations

We place the simulated binaries into environments representative of the real Universe. To achieve this, we allocate these systems to host galaxies produced by a cosmological simulation. We use the publicly available output from the Evolution and Assembly of GaLaxies and their Environments (EAGLE) project[7] (Crain et al. 2015; Schaye et al. 2015; McAlpine et al. 2016), specifically the RefL0100N1504 sample; the box size of $(100 \, \mathrm{Mpc})^3$ gives us a large, cosmologically representative volume to work with. Galaxies with stellar masses in the approximate range, $M_\star/\mathrm{M}_\odot > 10^8$, are considered well resolved and successfully reproduce the observed stellar galaxy mass function to $\lesssim 0.2$ dex (Furlong et al. 2015). We also include poorly resolved galaxies with masses close to the baryonic particle mass used in the simulation, $\sim 10^6 \, \mathrm{M}_\odot$ (Crain et al. 2015), to enable us to gauge the fraction of binaries that are seeded (see Section 2.3.1) into very small host galaxies, while recognizing that individual galaxy properties are not well determined in these cases.

The simulation is split into 28 non-uniformly spaced epochs spanning from $z \sim 15$ to $z \sim 0$. The use of EAGLE cosmological simulations allows binaries to be seeded in galaxies over cosmic time. These galaxies will undergo mergers and produce typically larger galaxies of varied morphologies (Qu et al. 2017) before the

binaries coalesce. Thus, by tracing the evolution of the binary systems within the evolving potential of the host, we can extract the galaxy properties when the compact binary coalesces.

2.3 Algorithm functionality

2.3.1 Binary seeding in EAGLE galaxies

For each cosmological epoch available in our selected EAGLE sample, we seed the simulated binaries in galaxies in proportion to their star formation rates and the averaged global metallicity. As the binaries form in discrete snapshots, a birth time offset is applied to create a continuous distribution of binary formation redshifts. Previous studies have used similar techniques to predict the morphology of binary merger host galaxies (e.g. Mapelli et al. 2018; Artale et al. 2019; Jiang et al. 2020).

Within zELDA, the binaries are seeded within their host galaxies at a distance that is weighted by the mass profile of the stellar disc. The evolution of the binary is traced from the birth of the progenitor massive stars to the point at which the final compact binary coalesces. The stellar evolutionary lifetime of each star is typically short ($\sim 10 \, \mathrm{Myr}$), and usually ends with a core-collapse supernova, leaving behind a compact remnant. Each supernova provides the system with a natal-kick velocity (Belczyński & Bulik 1999; Fragos et al. 2009; Giacobbo & Mapelli 2018). In some cases, the imparted impulse may disrupt the system entirely, and therefore, a compact binary is never created. For surviving compact binaries, the direction of the kick is applied to the entire system randomly with respect to the galactic plane. For sufficiently large kicks and long lifetimes, systems may migrate to great distances from their hosts before merging, consistent with the prevalence of SGRBs that are either apparently host-less or at large offsets on the sky from their likely hosts (e.g. Fong et al. 2013; Berger 2014; Tunnicliffe et al. 2014; Zevin et al. 2019; Gompertz, Levan & Tanvir 2020).

The overall star formation rate density within the EAGLE simulation is noted to be 0.2–0.5 dex lower than the observed rate density (Furlong et al. 2015). For the purpose of this study, we assume the star formation in different galaxy types reflects the real Universe (Madau & Dickinson 2014), despite the offset in the overall normalization. We stack the ordered EAGLE galactic star formation rates within a snapshot to obtain the cumulative star formation rate (CSFR). For each binary, a random value between zero and the maximum CSFR is then selected, and the corresponding galaxy is taken as the host. Galaxies with higher star formation rates, are therefore, more likely to host binaries. We use three sub-samples for the synthesized binaries. These consist of a low-metallicity ($Z = 0.004$), an intermediate-metallicity ($Z = 0.008$), and a high-metallicity ($Z = 0.02$) population (see Section 2.1.2). The binaries are seeded into galaxies based on the averaged star-forming gas metallicity, Z_{gal}. This quantity is allocated to bins corresponding to the three binary metallicity populations used. An associated binary from these populations is then selected and seeded into a binned host galaxy, i.e. low-met binaries are seeded in galaxies with $Z_{\mathrm{gal}} < 0.006$, intermediate binaries in galaxies with $0.006 \leq Z_{\mathrm{gal}} \leq 0.014$, and high-metallicity binaries in $Z_{\mathrm{gal}} > 0.014$. The binaries are drawn according to a Kroupa IMF (Kroupa 2001) profile for the primary stellar component.

Fig. 2 shows the population density of the seeded binaries as a function of τ_{merge}, the total system lifetime (i.e. stellar evolution plus in-spiral lifetimes), for all metallicities used. The relative fraction of binaries merging with a given lifespan varies between the type (i.e. NSNS or eBHNS) and the metallicity of the binary. The total natal-
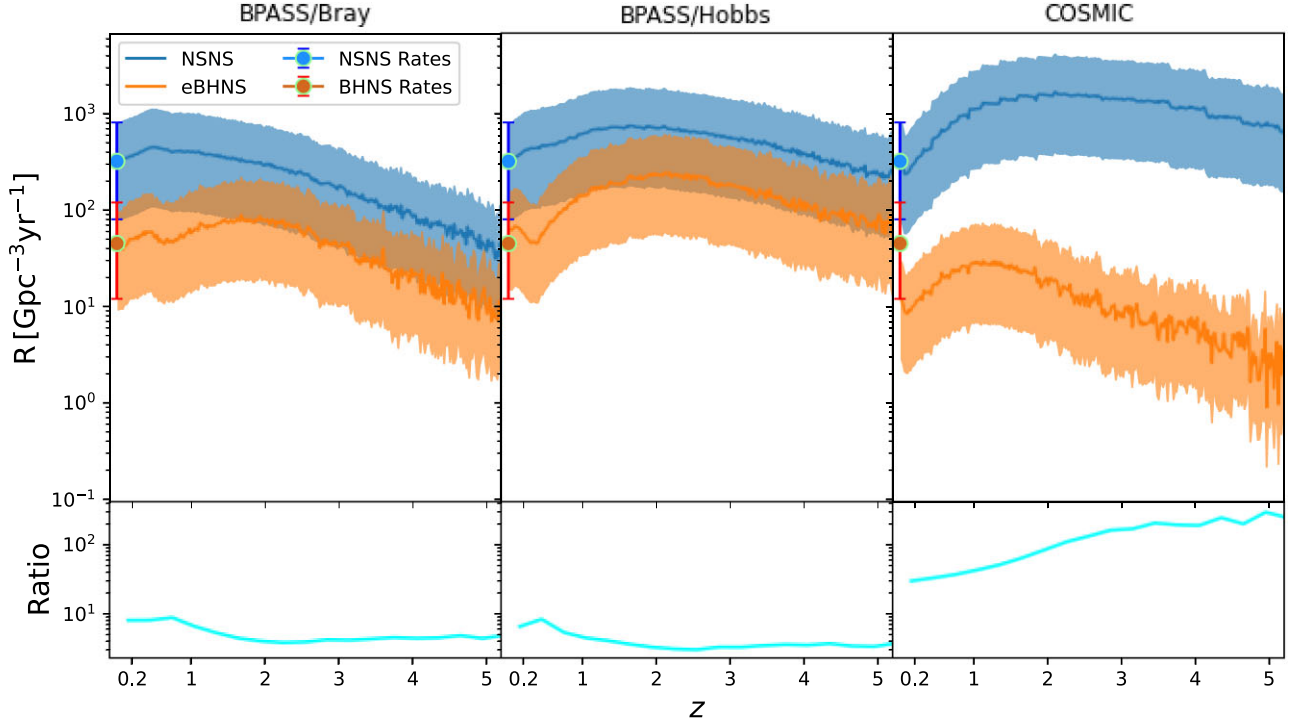
Figure 4. Comoving volumetric rate of NSNS (blue) and eBHNS (orange) compact binary mergers normalized by the local LIGO/Virgo gravitational wave rate, 320^{+490}_{-240} Gpc^{-3} yr^{-1} for NSNS systems (Abbott et al. 2021a). The shaded regions correspond to the rates contained within the upper and lower bound of the LIGO/Virgo estimate used. The cyan lines in the bottom panels show the relative ratio of NSNS against eBHNS systems. The plotted points correspond to the local volumetric rate estimates for NSNS, and BHNS (45^{+75}_{-33} Gpc^{-3} yr^{-1}) (Abbott et al. 2021b) mergers.

kick velocity distribution of the seeded NSNS and eBHNS binaries is shown in Fig. 3.

For the different binary evolution codes, the rate of merging compact binaries as a function of redshift is shown in Fig. 4. These rates have been normalized using the LIGO/Virgo O3 estimate of 320^{+490}_{-240} Gpc^{-3} yr^{-1} for the merger rate density of NSNS systems (Abbott et al. 2021a). The NSNS merger rate density always exceeds that of EM-bright eBHNS, but the ratio varies significantly between our three simulations, as demonstrated by the cyan lines in the figure.

2.3.2 Orbital evolution of kicked compact binaries within their host potentials

For binaries that remain intact, we trace their orbital evolution within their host galaxies. The morphology and potential of the galaxy evolves according to its descendant in the following EAGLE snapshots encountered during the lifetime of the orbit. The gravitational potential is modelled as a static well until the next snapshot, where it is updated if the host evolves or merges.

In our study, the global potential is composed of three contributors, a Navarro–Frenk–White (NFW; Navarro, Frenk & White 1996) profile for the dark matter halo, and two Miyamoto–Nagai (MN; Miyamoto & Nagai 1975) potentials for the stellar and gas bodies. The prescriptions for the galactic potential are scaled accordingly by the component masses for the EAGLE galaxies. The potential for the NFW profile is described by equation (1). The EAGLE simulation provides particle information corresponding to the galaxies which can be used to construct the gravitational potentials. However, this would be significantly more computationally expensive with little practical gain. As such, we do not expect a significant difference between the two methods when averaged over the total population

of galaxies.

$$\Phi(r) = -\frac{4\pi G \rho_0 R_s^3}{r} \ln\left(1 + \frac{r}{R_s}\right), \tag{1}$$

where G is the gravitational constant, ρ_0 is the central density, R_s the scale radius, and r is the radius from the central axis of the galaxy. R_s is fixed by requiring that the half-mass radius for the halo matches that reported in EAGLE. The MN potential on the other hand, is constructed with the following general prescription

$$\Phi(r, z) = \frac{-GM}{[r^2 + (a + (z^2 + b^2)^{1/2})^2]^{1/2}}, \tag{2}$$

where z is the height relative to the galactic plane, a is the scale-length, b is the scale height. Increasing the ratio of b/a dictates whether the geometry of the galaxy is more disc-like ($b < a$) or more spheroidal ($b \geq a$).

The MN potential (see equation 2) for the stellar distributions are created assuming a non-flat potential. We can approximate the scalelength, a, by applying a similar minimization for the half mass of the component as seen with the estimates of R_s. The scaleheight, b, is approximated using the relation, $b = a[(1 - \epsilon)/\epsilon]^2$, where ϵ is the stellar ellipticity for the EAGLE galaxy. A Milky Way-like galaxy has an approximate scale length ratio of $b/a \sim 0.1$.

The morphological structure can be quantified using the $\alpha_m = (\epsilon^2 + 1 - T)/2$ diagnostic described in Thob et al. (2019), where T is the triaxiality of the galaxy. We broadly distinguish early-/late-type morphologies based on a fiducial value of α. Galaxies with $\alpha_m \leq 0.4$, are assumed to be early-type galaxies, with late-types assumed to have $\alpha_m > 0.4$. We note that this is an essentially structural definition, and at higher redshifts other typical characteristics of early-type galaxies, such as low specific star formation rate, will not apply. For

Table 1. A population breakdown of EM bright compact binary mergers according to the probable observed host classification, for the binary simulations used. The bottom segment of the table compares the total simulated 'BAT-detectable' SGRB progenitors against the demographics breakdown of observed SGRBs from Fong et al. (2013). The square brackets indicate the demographics of systems expected to exhibit bright afterglows. A further breakdown of the host-less population is highlighted beneath the divisions for the 'NSNS', 'eBHNS', and 'BAT-detectable SGRB Progenitors' segments. Faint galaxies are defined as sources with a magnitude, $H > 26$, while binaries are considered remote if $P_{chance} > 0.05$.

Binary source	BPASS/Bray (per cent)	BPASS/Hobbs (per cent)	COSMIC (per cent)	Fong et al. (2013) (per cent)
		NSNS		
Early-type galaxies	26.5	20.8	26.5	–
Late-type galaxies	50.7	40.5	51.5	–
Total Obs. Host-less	22.9	38.7	22.1	–
Faint galaxies	0.9	1.4	5.8	–
Remote binaries	14.1	25.7	9.1	–
Faint Host + Remote	7.8	11.7	7.2	–
		eBHNS		
Early-type galaxies	29.6	25.0	19.3	–
Late-type galaxies	38.0	28.8	63.9	–
Total Obs. Host-less	32.4	46.2	16.8	–
Faint galaxies	1.5	2.9	1.8	–
Remote binaries	24.5	31.7	13.1	–
Faint host + remote	6.4	11.6	1.8	–
		BAT-detectable SGRB progenitors[a]		
Early-type galaxies	30.2 [31.4]	23.8 [30.0]	23.6 [25.1]	$\gtrsim$17
Late-type galaxies	50.6 [63.1]	41.5 [59.7]	61.0 [67.6]	$\approx$47
Total Obs. Host-less	19.2 [5.6]	34.8 [10.3]	15.5 [7.3]	$\gtrsim$17
Faint galaxies	0.3 [0.3]	0.6 [0.6]	2.7 [1.6]	–
Remote binaries	15.1 [4.5]	28.8 [8.6]	10.1 [4.3]	–
Faint host + remote	3.7 [0.8]	5.4 [1.2]	2.7 [1.5]	–

[a]The demographics fractions corresponding to a sub-population of SGRB progenitors merging in afterglow-bright environments (see Section 4.2).

galaxies where α_m can not be determined due to the absence of the required shape parameters, we use the red/blue sequence criterion discussed in Correa et al. (2017). This affects $\lesssim$ 5 per cent of the early-type galaxy classifications made.

The effects of galaxy mergers on the binary are approximated within ZELDA. If the host merges with a larger galactic dark matter halo, we apply a pseudo-kick equivalent to the maximum circular velocity of the major halo in a random direction to approximately account for the velocity offset entailed in switching to the new origin. Tidal interactions with the central supermassive black-holes of galaxies can also result in the disruption of binaries (Amaro-Seoane, Miller & Kennedy 2012; Mainetti et al. 2016). Similar effects may also arise from interactions with nearby gravitating bodies such as satellite galaxies. However, in the analysis underlined in this paper, we do not consider the effects of the central black hole or nearby neighbouring galaxies as the resulting gravitational intricacies from these are beyond the scope of this paper.

The orbital and galaxy dynamic prescriptions that are used in ZELDA incorporate functionality from the GALPY[8] PYTHON package, (Bovy 2015) using the relevant mass, radius, and shape properties from the EAGLE simulation.

3 HOST GALAXIES OF COMPACT BINARY MERGERS

Table 1 shows the host galaxy demographics broken down for each binary simulation. Figs 5, 6, 8–14 and Tables 2 and 3 correspond to

BPASS/Bray binaries. The equivalent results for BPASS/Hobbs and COSMIC are found in Appendices[9] A and B, respectively.

3.1 Galaxy host characteristics of coalescing binaries

The majority of binaries seeded within the EAGLE galaxies are born within $0.5 \lesssim z \lesssim 3$ and merge within $0 \lesssim z \lesssim 1$. The distribution of the merger time varies between different prescriptions for binary formation. This enables us to gauge the typical age and relative binary population as a function of redshift (Chruslinska, Nelemans & Belczynski 2019). The understanding of binaries merging within their host galaxy is also pivotal in providing insight into the chemical enrichment of the host galaxy (Shen et al. 2015; van de Voort et al. 2020). Similarly, ejected systems have relevance for our understanding of the enrichment of the intergalactic medium.

The successful association of a compact binary and its host galaxy can further yield constraints on the system's merger timescale, if the star formation history of the host is known (McCarthy, Zheng & Ramirez-Ruiz 2020). In Figs 5 (NSNS), and 6 (eBHNS), we show the relationship between the host galaxy mass and SFR at various redshift ranges for merging binaries. Colour coding shows the binary lifetimes. which range from 10s to 1000s of Myr. At lower redshift ($z < 1$), a large fraction of BPASS/Bray and BPASS/Hobbs merging binaries have lifespans of $\tau_{merge} > 1000$ Myr. These systems formed at earlier epochs ($z > 1$) within actively star-forming galaxies, but ultimately merge when the host is in a more quiescent phase.

[8]http://github.com/jobovy/galpy

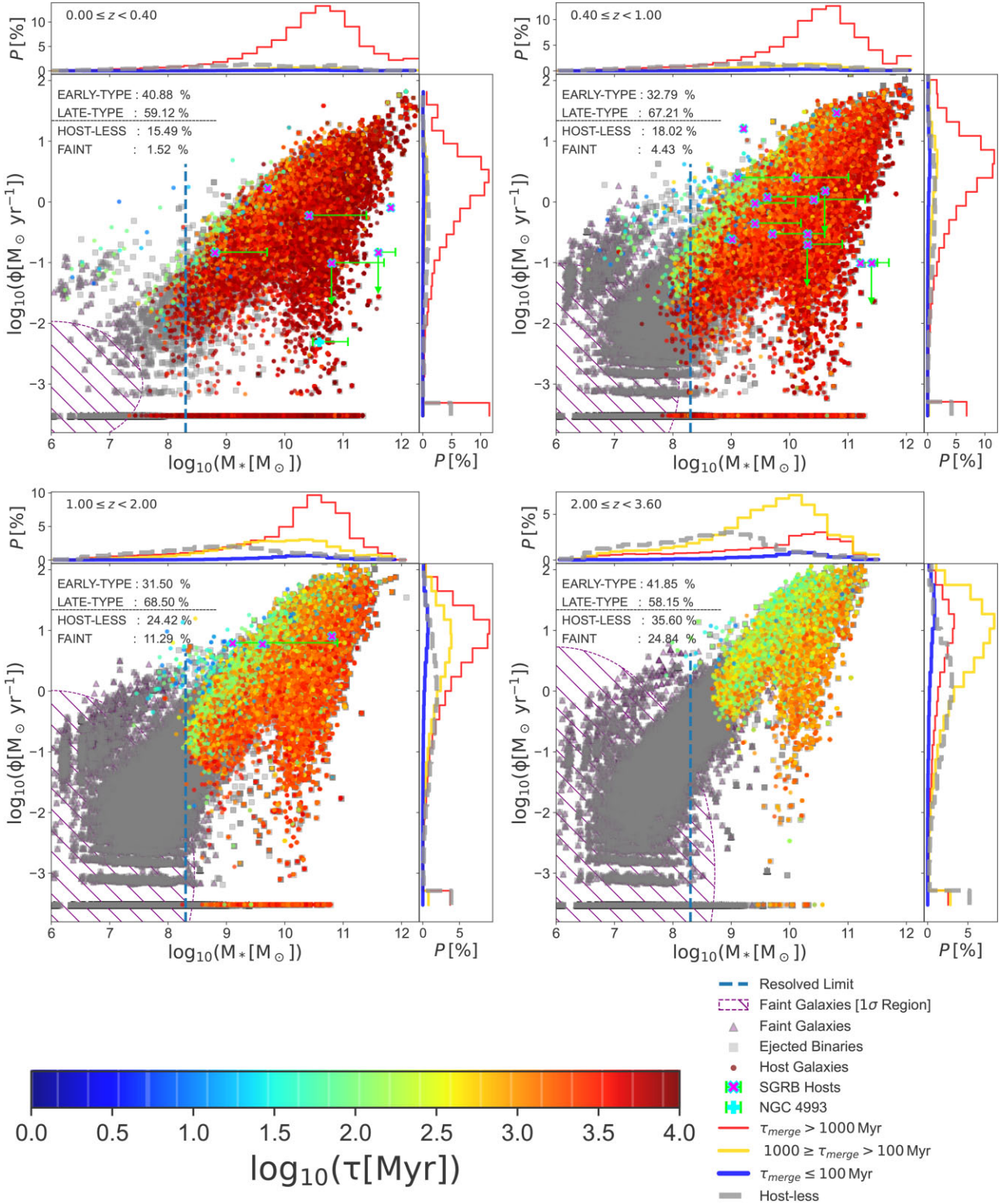[9]The appendices are available online on the journal website.

Figure 5. [BPASS/Bray – NSNS] The star formation rate (ϕ) against stellar mass (M_*) evolution of NSNS merger hosts. In each panel, the point colours represent the binary merger time. The vertical dashed line indicates the resolved threshold for EAGLE galaxies (see Section 2.2). The hosts of ejected binaries are represented in grey. Galaxies that are considered observationally faint (apparent magnitude $H > 26$) are depicted as purple triangles, the indicated hatched region within 1σ deviation from the mean ϕ and M_* of this population. The purple crosses indicate the host properties of localized SGRBs and their ϕ and M_* uncertainties, (Leibler & Berger 2010; Berger 2014). The cyan point corresponds to the galaxy (NGC 4993) that is the known of host of SGRB 170817A (Im et al. 2017; Levan et al. 2017) – the EM counterpart of the binary neutron star GW detection, GW170817. In each panel, the percentage of predicted late/early merger hosts are indicated. The estimated total population of host-less binaries (see Section 3.2.2) and faint hosts are also stated.
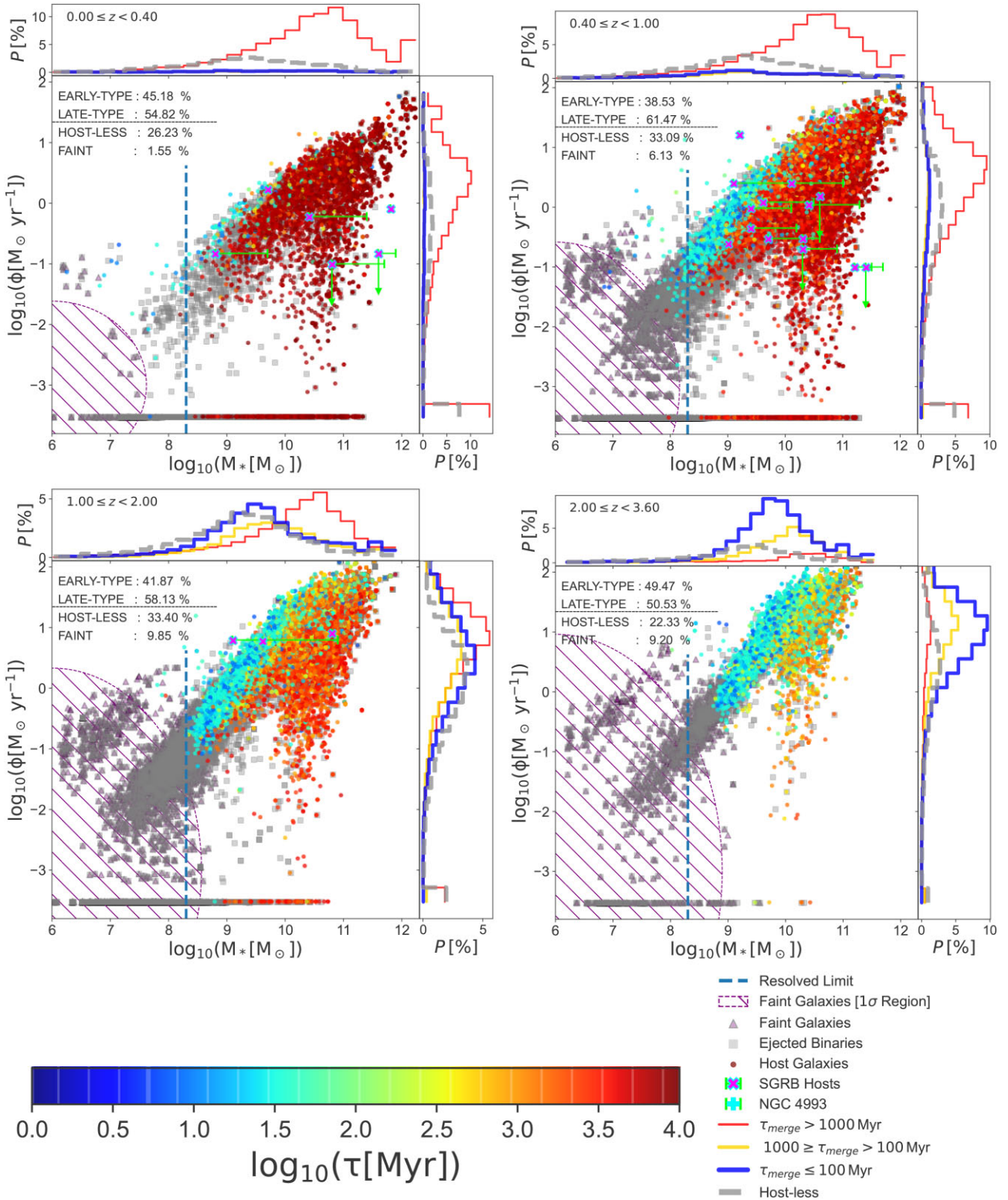
Figure 6. [BPASS/Bray – eBHNS] The star formation rate (ϕ) against stellar mass (M_*) evolution of eBHNS merger hosts. In each panel, the point colours represent the binary merger time. The vertical dashed line indicates the resolved threshold for EAGLE galaxies (see Section 2.2). The hosts of ejected binaries are represented in grey. Galaxies that are considered observationally faint (apparent magnitude $H > 26$) are depicted as purple triangles, the indicated hatched region within 1σ deviation from the mean ϕ and M_* of this population. The purple crosses indicate the host properties of localized SGRBs and their ϕ and M_* uncertainties, (Leibler & Berger 2010; Berger 2014). In each panel, the percentage of predicted late/early merger hosts are indicated. The estimated total population of host-less binaries (see Section 3.2.2) and faint hosts are also stated.
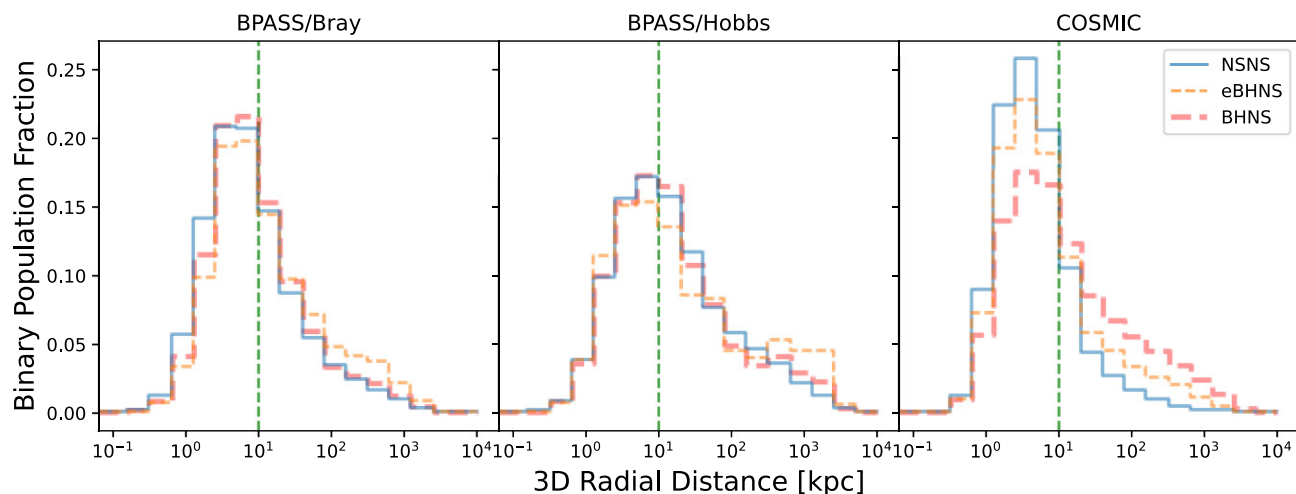
Figure 7. The population normalized (N/N_{bin}) migrated distance distributions over all redshifts, for the BPASS/Bray, BPASS/Hobbs, and COSMIC simulated NSNS (blue) and eBHNS (orange) compact binaries. The fainter red lines correspond to the total population of seeded binaries, inclusive of non-bright EM systems (refer to Section 2.1.2). Relative to the COSMIC binary models sampled over, fewer unique BPASS models are used within our simulation. The resolution of the binned population is therefore limited∗. ∗Secondary and tertiary peaks are artefacts of noise. The green dashed line corresponds to a distance of 10 kpc.

Coalescing binaries within $z < 0.4$ have host galaxies with a median stellar mass between $M_* \sim 1.5$–$3 \times 10^{10} M_\odot$, and a star formation rate within the range $\phi \sim 1.3$–$2.1 M_\odot yr^{-1}$. These galaxies tend to be massive, star-forming, and disc dominated (e.g. Calvi et al. 2018). For comparison, the Milky Way has a stellar mass, $M_* \sim 6 \times 10^{10} M_\odot$, and a star formation rate of, $\phi \sim 1.6 M_\odot yr^{-1}$ (Licquia & Newman 2015). The purple crosses marked in Figs 5 and 6 indicate the properties of galaxies associated with localized SGRB detections, for the subset of cases for which these host parameters have been estimated. Generally, the majority of these galaxies are consistent with the expected hosts of merging compact objects predicted by zELDA. For the lowest redshift slice, the overplotted properties of the host galaxies reside below the peak of the host distributions. We note that intrinsically very faint hosts may be missed, or unidentified, in follow-up observations, so their absence in the observed sample may not be surprising. The properties of the NSNS merger host associated with GW170817, NGC 4993, falls within a region where very few galaxies are expected to host coalescing NSNS systems. An event such as this is rare based on the zELDA predictions.

We distinguish between early and late-type host galaxies at the point of coalescence based on the morphological criteria described in Section 2.3.2. Approximately 50–70 per cent of mergers for BPASS compact binaries appear to originate from late-type galaxies at all redshifts in each simulation. For the COSMIC sample, the fraction of binary mergers originating from late-type hosts can range up to ∼ 80 per cent. We note that Artale et al. (2020a) performed a similar simulation based on EAGLE, and concluded that at low redshifts ($z < 0.1$) early-type galaxies dominate the host population. However, the discrepancy between our studies is due to a different approach in distinguishing galaxy morphologies. Specifically, they define early-type galaxies to have specific star formation rates, $SFR/M_* < 10^{-10} yr^{-1}$. This means that many galaxies that we classify as late-type discs at low redshifts are considered early-types within their work based on their star formation rate criterion.

A non-negligible fraction of these binaries are shown to migrate to distances where they are considered to be host-less (elaborated on in Section 3.2.2); the host galaxies for these systems are depicted as grey squares in Figs 5 and 6. The figures also indicate galaxies that

could be missed with an observational follow-up, as they are faint ($H > 26$; purple triangles). Small spiral/dwarf galaxies, and more distant intrinsically brighter galaxies, are likely to fall into this category due to their low apparent luminosity. The overall galaxy demographics including the contribution of host-less systems is shown in Table 1.

3.2 Projected galactocentric distance at merger

3.2.1 The impact parameter

By following the evolution of binaries from their birth to their coalescence, we are able to observe the overall migration distance during their lifetimes. In our simulations, these are turned into projected on-sky distances by choosing random orientations for each host galaxy and calculating the corresponding impact parameter.

Fig. 7 shows the global distribution of the migration distances that the NSNS and eBHNS mergers exhibit for the various population synthesis codes used. We find ∼ 60–70 per cent of NSNS and eBHNS mergers occur within ≲ 10 kpc (indicated by the vertical dashed line) from the centre of their host galaxies, for BPASS/Bray binaries. For BPASS/Hobbs binaries, ∼ 50 per cent of binaries are retained within this distance. For COSMIC binaries, ∼ 70–80 per cent of systems merge within this distance. In extreme cases, we find ≲ 1 per cent of these binaries merging at galactocentric distances > 1 Mpc for BPASS/Bray and COSMIC binaries, and ≲ 5 per cent for the BPASS/Hobbs population.

Figs 8 and 9 show the impact parameter distributions, where the impact parameter corresponds to the projected on-sky separations, split by the host galaxy characteristics (stellar mass and star formation rate) and redshift. Generally, binaries with high velocities have a higher likelihood of overcoming the gravitational potential of their host galaxy and thus travelling further before coalescing. For low-mass galaxies such as small disc or dwarf galaxies, the likelihood increases as the gravitational potential is weaker and therefore, easier to escape. As such, these galaxies are expected to retain very few binaries. We see this for both NSNS and eBHNS systems in the top panels of both figures.

For binaries merging in larger galaxies such as large spirals (middle and bottom panels) or ellipticals (bottom panel), the
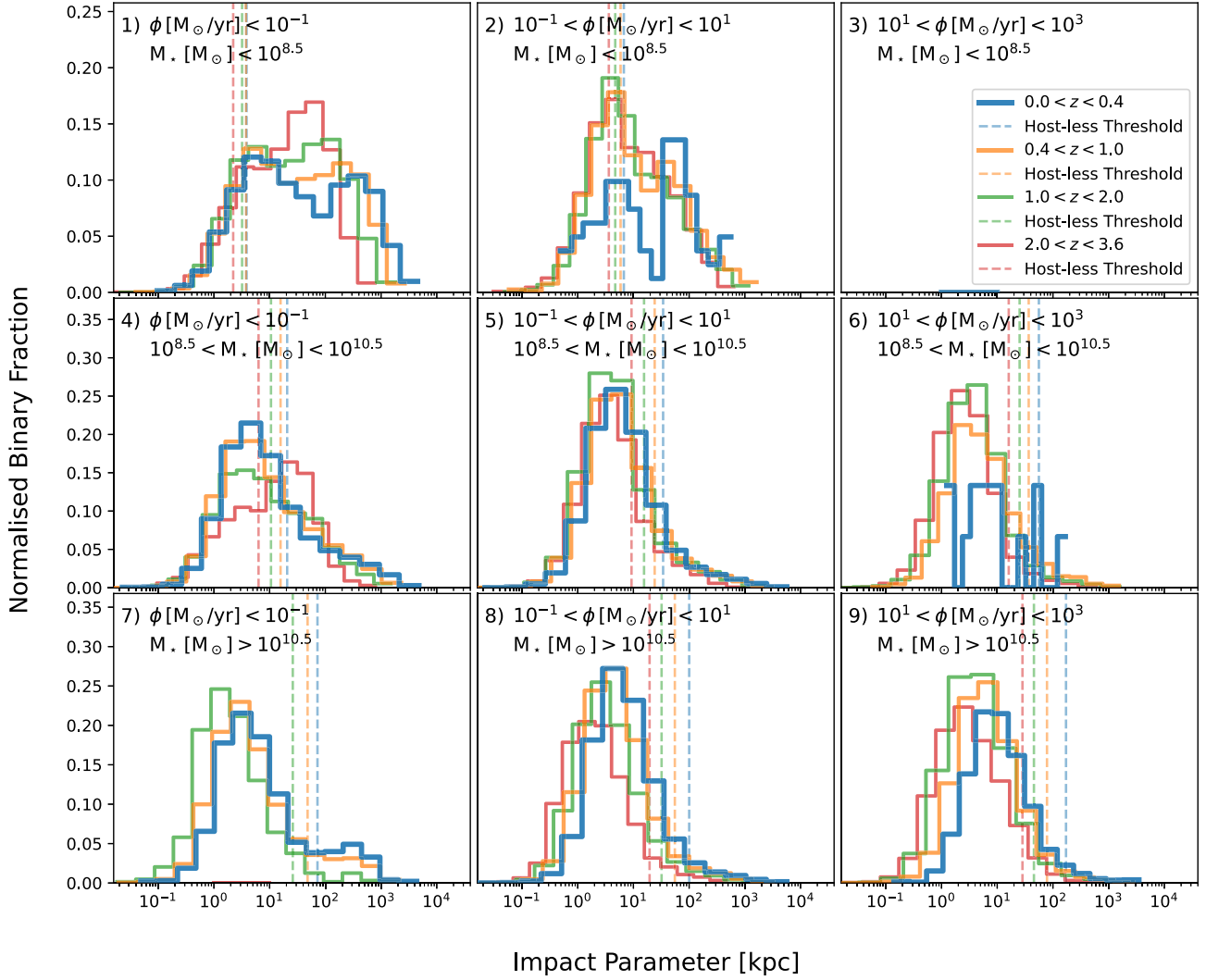
Figure 8. [BPASS/Bray – NSNS] For varied redshift slices, each panel corresponds to a breakdown of the impact parameter distributions for different galaxy masses (row), and star formation rates (column). Each histogram is composed of the number of binaries with a given impact parameter normalized over the total summation of merging systems within the respective panel and redshift. The dashed vertical line corresponds to the galaxy averaged impact parameter corresponding to the P_{chance} limit used to identify systems that may be potentially classed as host-less. A numerical breakdown of each panel is shown in Table 2.

coalescence is likely to occur within $\sim 10\,\mathrm{kpc}$ and therefore, close to or within the host galaxy. Tables 2 and 3, show the fractions of binaries merging in each panel per redshift slice, corresponding to the aforementioned figures.

3.2.2 Chance alignment of binaries and their host galaxies

A binary is considered host-less if the offset from its host is likely to be observationally registered as a chance alignment, with a probability, $P_{chance} > 0.05$ (e.g. Fong et al. 2013) and/or if the host is fainter than $H > 26$. The P_{chance} quantity is calculated using the prescription for chance alignments from Bloom et al. (2002) and defined as

$$P_{chance} = 1 - e^{-\eta}, \tag{3}$$

where

$$\eta = \pi r_i^2 \sigma(\leq m). \tag{4}$$

Here, r_i is an angular distance that is determined based on the offset of a binary merger relative to the centre of its host, and the size of the

galaxy. Specifically, if a binary merger occurs at a projected radius less than twice the projected half mass stellar radius (R_*) of its host galaxy, it is assumed to be 'within' the host and r_i is set to $r_i = 2R_*$. For mergers occurring further out from their host galaxy centre $r_i = \sqrt{R_0^2 + 4R_*^2}$, where R_0 is the angular offset between the centre of the host and the site of the merger. $\sigma(< m)$ is the mean surface density of galaxies brighter than the H-band magnitude (m) of the host galaxy.

Our procedure differs slightly from the original Bloom et al. (2002) prescription in that we use the projected half-mass stellar radius in place of the half-light radius; and we use H-band rather than r-band magnitudes as early-type galaxies in particular tend to become rapidly fainter in the r band at $z \gtrsim 1$ due to the redshifting of the 4000 Å break through the filter passband. H band number counts for field galaxies are taken from Metcalfe et al. (2006), Frith, Metcalfe & Shanks (2006), and we use a polynomial interpolation between the values to extract the mean surface density for any H-band magnitude. In the context of our simulations, we use the given apparent magnitude of the host galaxies reported by EAGLE.
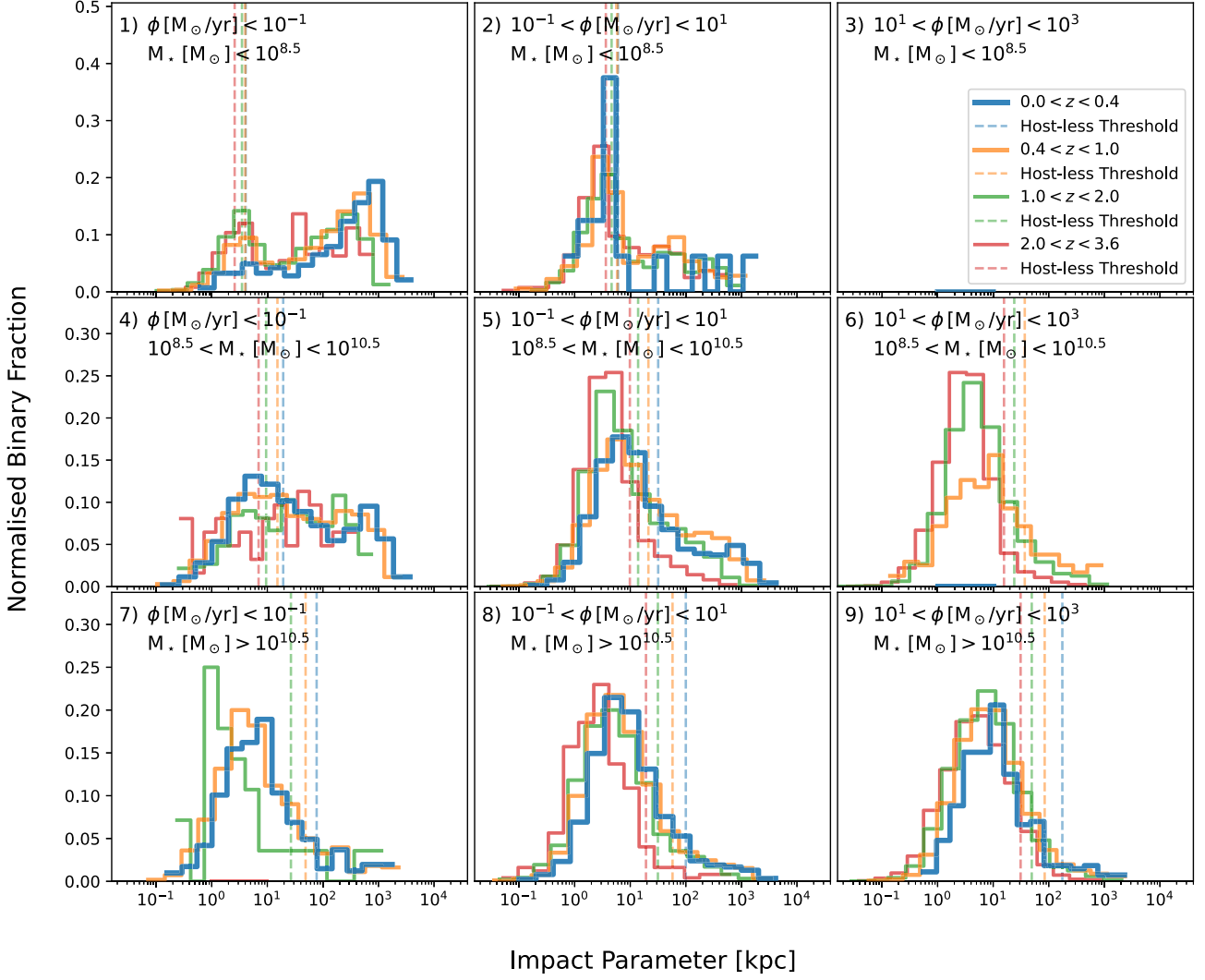
Figure 9. [BPASS/Bray – eBHNS] For varied redshift slices, each panel corresponds to a breakdown of the impact parameter distributions for different galaxy masses (row), and star formation rates (column). Each histogram is composed of the number of binaries with a given impact parameter normalized over the total summation of merging systems within the respective panel and redshift. The dashed vertical line corresponds to the galaxy averaged impact parameter corresponding to the P_{chance} limit used to identify systems that may be potentially classed as host-less. A numerical breakdown of each panel is shown in Table 3.

The $H > 26$ criterion accounts for hosts that appear faint (particularly those at higher redshift) and therefore are likely to be missed when following up SGRBs, resulting in them being classified as host-less by observers. Recognizing the existence of these cases is essential when accounting for potential observational biases that can arise with SGRB samples.

The total fraction of NSNS and eBHNS that will appear to be host-less is shown in Table 1 for each binary simulation used. A breakdown of the fraction of binaries that fulfill our host-less criteria is shown for each panel of Figs 8 and 9 within the second sections of Tables 2 and 3.

4 SIMULATING OBSERVATIONAL SELECTION EFFECTS

4.1 Luminosity function and selection

We produce a simulated population of observable SGRBs assuming the broken power-law intrinsic luminosity function for SGRB peak

luminosities from Paul (2018)

$$\Phi(L) \propto \begin{cases} \left(\frac{L}{10^{52.18} \, \text{erg s}^{-1}}\right)^{-0.5} & L \leq 10^{52.18} \, \text{erg s}^{-1}, \\ \left(\frac{L}{10^{52.18} \, \text{erg s}^{-1}}\right)^{-1.86} & L > 10^{52.18} \, \text{erg s}^{-1}. \end{cases} \quad (5)$$

A broken power law is consistent with the findings in Wanderman & Piran (2015), Ghirlanda et al. (2016); alternatively, see Yonetoku et al. (2014), Sun, Zhang & Li (2015) for examples of single power-law luminosity functions. As the distribution of intrinsically low-luminosity SGRBs is poorly constrained, we fix the cut-off at $10^{49} \, \text{erg s}^{-1}$ (Mogushi, Cavaglià & Siellez 2019). As such, the luminosities, L, are drawn from a distribution within the range $10^{49} \leq L \leq 10^{55} \, \text{erg s}^{-1}$. The ascribed SGRB luminosity has no dependence on the binary characteristics, since we lack any theoretical or observational mapping that would motivate this. Whilst some SGRBs, such as GRB 170817A, exhibit luminosities below our minimum, these events are expected to account for a small fraction of the cumulative observed population (Tan & Yu 2020). We use a sensitivity of $0.2 \, \text{ph s}^{-1} \, \text{cm}^{-2}$ to estimate the fraction of GRBs that
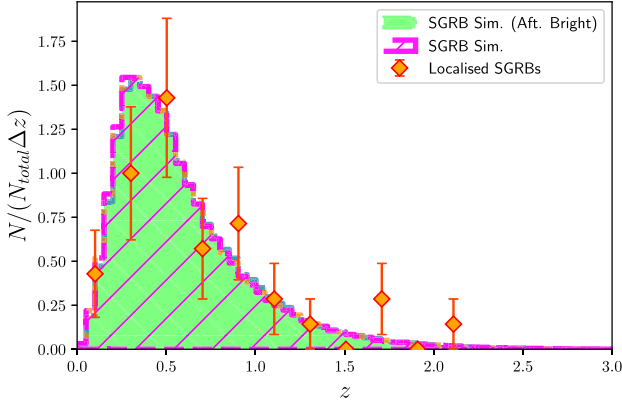
Figure 10. [BPASS/Bray] The distribution of the NSNS and eBHNS binary mergers from our study that is likely to produce SGRBs detectable by *Swift*/BAT, excluding host-less systems, refer to Section 3.2.2. The magenta histogram outlines the total population of BAT-detectable SGRBs with identifiable hosts. The lime histograms corresponds to the subset of events merging in afterglow-bright environments, $(n > 10^{-4}\,\mathrm{cm}^{-3})$. The orange points correspond to the population of *Swift* observed SGRBs within redshift bin sizes of $z = 0.2$, with a Poisson uncertainty.
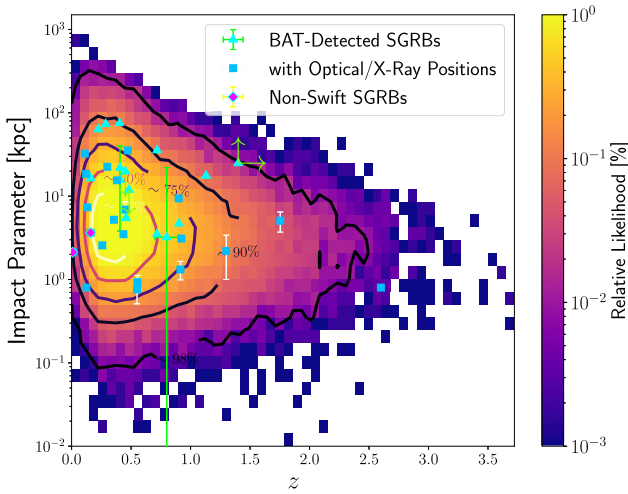

Figure 11. [BPASS/Bray] A density map of the impact parameter and redshift for binaries that are expected to produce an SGRB within *Swift*/BAT's detection sensitivity range and are not considered host-less (see Section 3.2.2). In both cases, offsets and redshifts corresponding to SGRB-galaxy from literature are plotted with their relevant uncertainties, refer to Table 5. The contour levels shown, proceeding outwards, indicate the $\sim$ 25, 50, 75, 90, and 98 per cent enclosed synthetic merging binary population. The total binary population is comprised of both NSNS and eBHNS binaries.

would be detectable by *Swift*/BAT. We apply a Band function (Band et al. 1993) with an index $\alpha = 0.5$ and $\beta = 2.25$ for the distribution below and above E_P, respectively, where E_p is the spectral peak energy given by the relation for SGRBs found by Tsutsui et al. (2013).

4.2 Afterglow dependence on environment

GRB afterglows are thought to arise when the relativistic jet impacts and shocks the external ambient medium, producing long-lived emission from radio to X-ray (Zhang et al. 2006, 2007). Identification of candidate host galaxies, and hence redshifts and impact
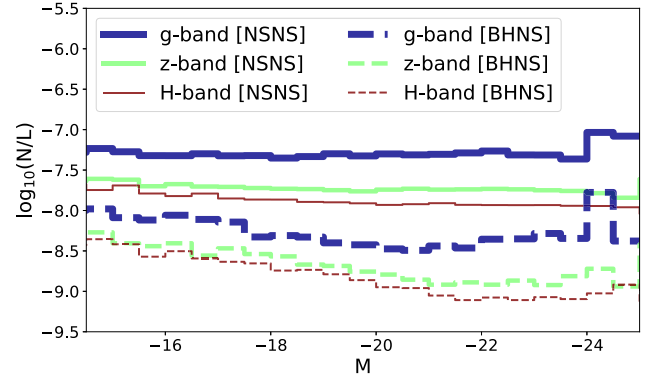

Figure 12. The ratio of NSNS (solid) and eBHNS (dashed) mergers (N) per unit luminosity (L) in bins of absolute magnitude, for all galaxies in the simulation volume (restricted to redshift $z < 0.05$, and the BPASS/Bray model). Shown are results for the $g/z/H$ band: of these, the g band is generally flatter, indicating that merger rate is, on average, more nearly directly proportional to luminosity in this band. Note that the luminosity scale here is arbitrary, so there is no particular significance to the relative values of N/L.

parameters, relies on the $\sim$arcsec localizations that come from X-ray and optical/nIR detections, rather than the $\sim$arcmin positions that are produced by the *Swift*/BAT. For some SGRBs, particularly those with 'extended soft emission' (Mészáros & Rees 1997; Sari, Piran & Narayan 1998), the X-ray localization may be found independently of afterglow detection, however, more commonly observations of the afterglow is necessary. Thus there is the possibility that SGRBs in low density environments may be selectively lost from the observational sample we consider here. In this section, we outline an approach to introduce this into the simulations, which may indicate a plausible maximum size of this selection bias.

The average gas density, n, surrounding a galaxy will decrease with increasing distance from the galaxy core, therefore, the afterglows from bursts at large separations from their host will typically have fainter afterglow emission (Perna & Belczynski 2002). The maximum luminosity distance, D_{max}, for the peak afterglow emissions to be above a given threshold depends on the ambient density as $D_{\mathrm{max}} \propto n^{(p+1)/8}$ assuming slow-cooling and an observed frequency above the characteristic synchrotron frequency at the peak, where p is the relativistic electron distribution index in the shock – typically $p \sim 2.4$ (Fong et al. 2015a). The afterglows of SGRBs can be used to put constraints on the ambient density, where the earliest afterglow detection can be used to constrain the minimum density. Using this minimum ambient density and an assumed galaxy gas density profile, O'Connor, Beniamini & Kouveliotou (2020) infer a maximum impact parameter distribution for the population of observed SGRBs.

For binaries capable of producing an SGRB e.g. NSNS, and eBHNS systems, (see Section 2.1.2), we estimate the fraction that merge in a very low density environment, defined by Fong et al. (2015a) as $n < 10^{-4}\,\mathrm{cm}^{-3}$. Based on the location of the merger with respect to its host galaxy, we estimate the ambient density by considering the gas mass contained within an EAGLE aperture. These apertures are composed of spheres with sizes of 1, 3, 5, 10, 20, 30, 40, 50, 70, and 100 kpc. We split these spheres into shells based on the radii of neighbouring apertures and calculate the spherically averaged gas density. We added an additional hot gas component, similar to the approach described in O'Connor et al. (2020). This secondary component is described by the Maller & Bullock gas
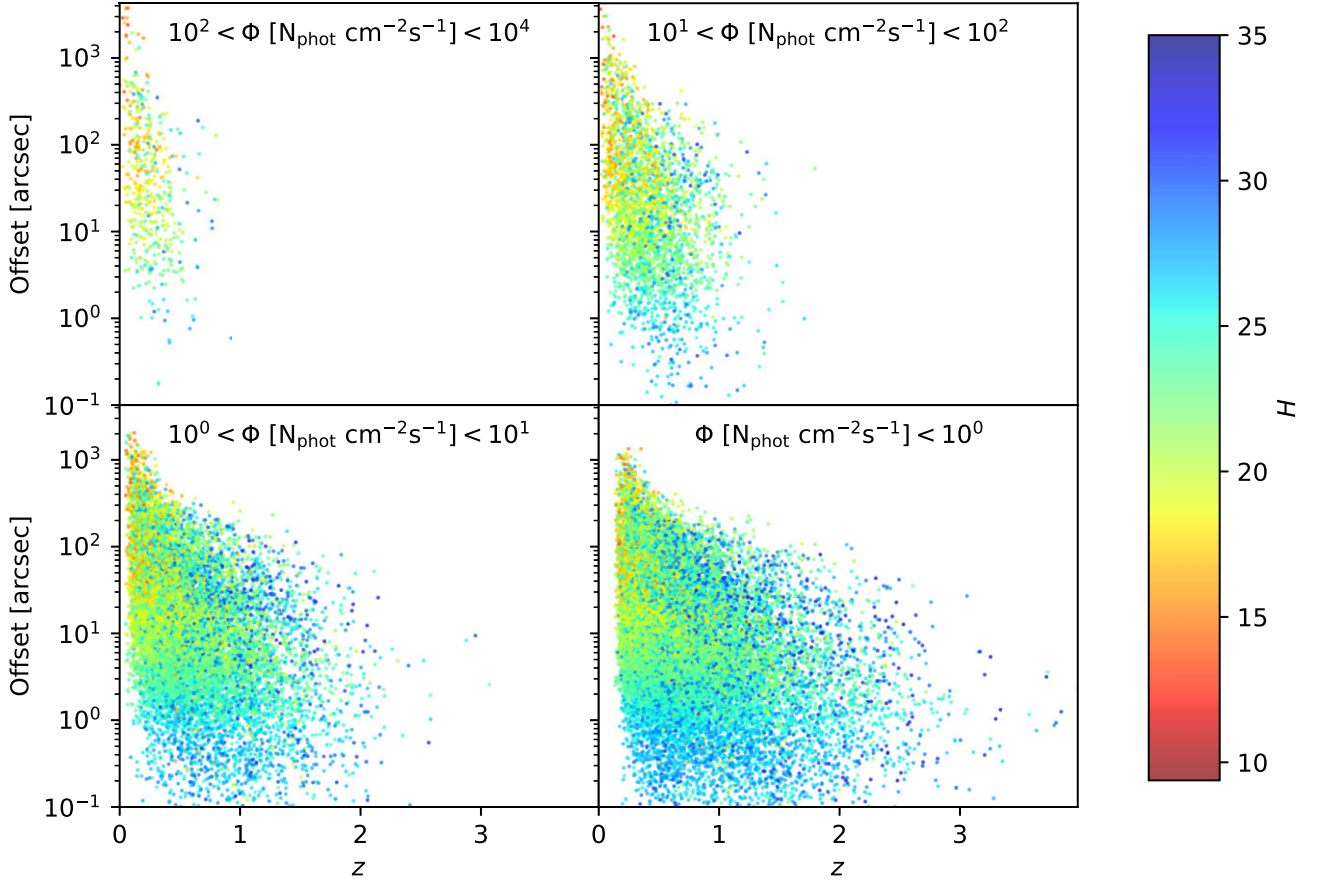
Figure 13. [BPASS/Bray] The distribution of host-less (see Section 3.2.2) binary merger offsets against redshift, z, corresponding to different ranges of photon flux, Φ. The colour of the points indicate the brightness of the host galaxy within the H band, with redder points indicating brighter host galaxies than the bluer points.
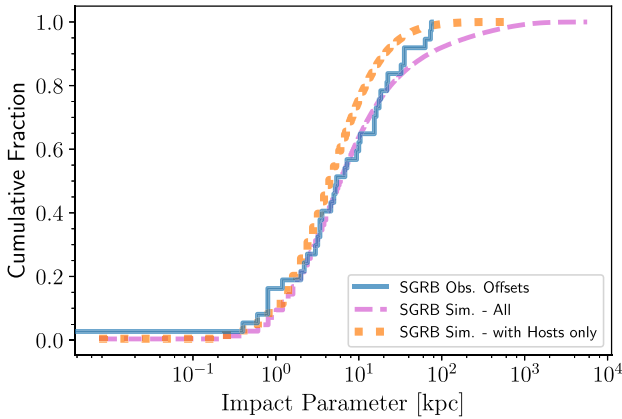

Figure 14. [BPASS/Bray] The impact parameter distribution for the population of SGRB compatible NSNS and eBHNS binaries expected to be observable by *Swift*/BAT for (i) all systems (lilac dashed), (ii) systems with hosts only (orange dotted). The blue line corresponds to a sample of SGRBs with known redshifts and offsets (blue) inclusive of non-*Swift* detected events. Refer to Table 5 for sources used.

model (Maller & Bullock 2004; Fang, Bullock & Boylan-Kolchin 2013),

$$\rho_g^{MB}(x) = \rho_v \left[1 + \frac{3.7}{x}\ln(1+x) - \frac{3.7}{c_v}\ln(1+c_v) \right]^{3/2}, \qquad (6)$$

where ρ_v is the density at the virial radius, r_v (Carlberg et al. 1997), corresponding to an overdensity parameter of $\Delta_v = 200$; x is the ratio of r/R_s; and c_v is the concentration parameter (e.g. Bullock et al. 2001; Comerford & Natarajan 2007). Using this prescription, we identify the fraction of the SGRB progenitor mergers that occur in environments with $n < 10^{-4}\,\mathrm{cm}^{-3}$ as afterglow-faint. Mergers occurring in denser environments are considered to be afterglow-bright.

The total population of the simulated SGRB progenitors merging in environments with low ambient densities is shown in the first half of Table 4. This is further split according to whether the merger fulfills our criteria for being host-less or not. The proportion of mergers occurring in low density media is therefore somewhat increased over the whole population. Notably, the proportion of host-less BAT-detectable SGRBs formed by COSMIC and BPASS/Bray binaries merging within afterglow-faint environments are broadly consistent, within errors, with the estimated fraction of SGRBs occurring in a $n < 10^{-4}\,\mathrm{cm}^{-3}$ ambient density medium by O'Connor et al. (2020), whereas the ≈ 35 per cent fraction of SGRBs in low density environments predicted by the BPASS/Hobbs simulation is rather in excess of the observations.

In Fig. 10, we compare the redshift distribution of observed SGRBs against our predictions for the BAT-detectable mergers with host associations. The agreement is generally reasonable, although the finding of several SGRBs at $z \gtrsim 1.7$ is harder to reconcile with the small numbers predicted at those redshifts. This may suggest that the bright-end slope of our adopted luminosity function (equation 5) is rather too steep.

Table 2. [BPASS/Bray – NSNS] A breakdown of the relative binary mergers occurring within each panel of Fig. 8. The top division refer to the relative fractions of binaries coalescing for a given redshift slice. The last column indicates the population of the binaries contained within each slice as a percentage of the cumulative population. The second section of the table shows the estimated host-less population per panel [overall fraction corresponding to the redshift slice] based on the criteria defined in Section 3.2.

z	1	2	3	4	5	6	7	8	9	Total population (per cent)
				Binary fraction (per cent)						
$0.0 < z < 0.4$	4.6	0.1	0.0	9.9	33.9	0.0	5.5	38.0	8.0	10.6
$0.4 < z < 1.0$	5.4	0.5	0.0	5.5	39.8	0.9	2.2	28.8	17.0	42.4
$1.0 < z < 2.0$	7.8	2.2	0.0	2.1	43.8	7.6	0.2	11.8	24.5	36.5
$2.0 < z < 3.6$	11.4	6.0	0.0	0.9	41.4	22.4	0.0	2.4	15.6	10.5
				Host-less fraction/panel [Relative to z-slice] (per cent)						Total host-less fraction (per cent)
$0.0 < z < 0.4$	86.8 [4.0]	67.9 [0.1]	0.0 [0.0]	34.2 [3.4]	14.9 [5.0]	13.3 [0.0]	14.8 [0.8]	5.3 [2.0]	2.8 [0.2]	15.5
$0.4 < z < 1.0$	90.5 [4.9]	65.9 [0.3]	0.0 [0.0]	40.8 [2.2]	18.9 [7.5]	9.4 [0.1]	12.1 [0.3]	6.3 [1.8]	5.2 [0.9]	18.0
$1.0 < z < 2.0$	93.1 [7.2]	76.8 [1.7]	0.0 [0.0]	51.3 [1.1]	25.9 [11.4]	7.8 [0.6]	6.0 [0.0]	7.3 [0.9]	6.5 [1.6]	24.4
$2.0 < z < 3.6$	96.5 [11.0]	86.2 [5.1]	25.0 [0.0]	67.9 [0.6]	37.3 [15.4]	8.5 [1.9]	0.0 [0.0]	6.8 [0.2]	8.7 [1.4]	35.6

Table 3. [BPASS/Bray – eBHNS] A breakdown of the relative binary mergers occurring within each panel of Fig. 9. The top division refer to the relative fractions of binaries coalescing for a given redshift slice. The last column indicates the population of the binaries contained within each slice as a percentage of the cumulative population. The second section of the table shows the estimated host-less population per panel [overall fraction corresponding to the redshift slice] based on the criteria defined in Section 3.2.

z	1	2	3	4	5	6	7	8	9	Total population (per cent)
				Binary fraction (per cent)						
$0.0 < z < 0.4$	5.5	0.2	0.0	12.3	31.4	0.0	5.3	35.2	10.1	8.5
$0.4 < z < 1.0$	7.3	1.2	0.0	5.8	42.4	0.8	1.9	24.0	16.6	31.5
$1.0 < z < 2.0$	5.4	2.9	0.0	1.5	54.2	8.9	0.1	6.9	20.1	44.1
$2.0 < z < 3.6$	2.5	2.7	0.0	0.4	43.1	32.6	0.0	1.7	17.0	15.9
				Host-less fraction/panel [Relative to z-slice] (per cent)						Total host-less fraction (per cent)
$0.0 < z < 0.4$	93.9 [5.2]	56.2 [0.1]	0.0 [0.0]	55.9 [6.9]	31.8 [10.0]	0.0 [0.0]	10.8 [0.6]	8.9 [3.1]	3.6 [0.4]	26.2
$0.4 < z < 1.0$	90.0 [6.6]	58.9 [0.7]	0.0 [0.0]	59.5 [3.5]	41.4 [17.5]	18.6 [0.1]	15.7 [0.3]	12.1 [2.9]	8.7 [1.4]	33.1
$1.0 < z < 2.0$	87.7 [4.8]	69.2 [2.0]	0.0 [0.0]	69.6 [1.0]	38.7 [21.0]	14.5 [1.3]	17.9 [0.0]	13.7 [0.9]	11.7 [2.4]	33.4
$2.0 < z < 3.6$	91.5 [2.3]	68.2 [1.9]	0.0 [0.0]	64.5 [0.3]	29.6 [12.8]	8.3 [2.7]	0.0 [0.0]	8.1 [0.1]	13.5 [2.3]	22.3

Table 4. Summary of the fractions of SGRB progenitors merging in environments with ambient densities $< 10^{-4}$ cm^{-3}, for each binary simulation used. Systems are considered host-less if the host galaxy has a magnitude, $H > 26$, and/or if the offset of the binary is such that $P_{chance} > 0.05$.

Binary simulation	All SGRB progenitors (per cent)			BAT-detectable (per cent)		
	With host	Host-less	Total	With host	Host-less	Total
BPASS/Bray	4.9	14.9	19.9	9.3	14.8	24.2
BPASS/Hobbs	2.9	26.1	29.0	7.0	28.1	35.0
COSMIC	1.7	8.9	10.6	3.6	9.1	12.7

5 IDENTIFYING THE HOST GALAXIES OF SGRBS

5.1 Comparing study predictions against observations

Binaries capable of producing SGRBs within the sensitivity threshold of *Swift*/BAT are shown in Fig. 11. We have overlaid offset and redshift information for SGRBs noted in literature. There is a relatively high concentration of ZELDA processed binaries at redshift ~0.5 with relatively low impact parameters, ~ 10 kpc. The observed localized SGRBs tend to cluster at low redshift ($z \lesssim 1$) with spatial offsets < 100 kpc from their likely hosts. This is found to be consistent with the peak concentration predicted by the binary simulations used.

The identification of the parent galaxy associated with an SGRB is often non-trivial, especially for events with no bright galaxies in or near their localization uncertainty region, or in cases where no arcsec level localization was obtained in the first place. Campaigns aiming to successfully isolate and identify the hosts of these events have been ongoing throughout the *Swift* era (e.g. Levan et al. 2007; Berger 2009; Fong et al. 2013; Berger 2014). A host that has a low-apparent luminosity may easily be missed when searching within or around the localization uncertainty of a given SGRB detection. Apart from the rare cases where the SGRB is located on or close to an obvious bright (typically low redshift) galaxy, the first requirement is to conduct a deep-imaging of the field of sky surrounding the region of the burst. This is often provided by follow-up imaging of

the afterglow following the SGRB. Ultimately, associations made between the burst and the host galaxy is probabilistic given that the galaxy could be within the localized field by chance, see Section 3.2.2.

Fong et al. (2013) analysed the host demographics for 36 well associated SGRBs (i.e. events with convincing host galaxies backed by afterglow observations), finding that ~47 per cent have late-type hosts, ~17 per cent early-type, ~17 per cent host-less, and ~19 per cent are 'inconclusive' owing to their uncertain association with a nearby galaxy. Comparing our predictions (refer to the final segment of Table 1) with these values we find reasonably consistent fractions for SGRBs arising from late-type galaxies (e.g. BPASS/Bray: ~ 51 per cent). For the early-type hosts we predict a higher fraction (e.g. BPASS/Bray: ~ 30 per cent), although given the limited statistics, and the possibility that some of the 'inconclusive' cases could in fact be early-type hosts, we do not think this is a serious discrepancy. Similarly, the host-less population fraction of BAT-detectable SGRBs only slightly varies from the Fong et al. (2013) numbers for the BPASS/Bray and COSMIC simulations, which could easily be accounted for if some 'inconclusive' cases are ultimately considered host-less, combined with the observational selection bias against localizing afterglow-faint SGRBs since they are also more likely to be host-less (cf. Table 4). For BPASS/Hobbs, the ~35 per cent host-less fraction is only consistent with the observed population if the majority of the 'inconclusive' population from Fong et al. (2013) is considered host-less.

5.2 Implications for host searches for GW detected events

The rich science returns from observations of neutron–star compact binary mergers in both gravitational waves and electromagnetic radiation has been exemplified by the case of GW170817 (e.g. Abbott et al. 2017a, b). However, even with the current three advanced GW detectors, positional error regions are typically 10s or 100s of sq-deg in size, while the distance range for such events is ~ few $\times 10^2$ Mpc (Abbott et al. 2018). This is challenging both in terms of sky area and depth required to locate EM counterparts, apart from the rare cases of on-axis SGRBs. To aid in mapping these error regions, particularly with narrow-field optical, near-IR or X-ray instruments, various strategies have been suggested to prioritize observations based on the known positions and properties of potential host galaxies (e.g. Evans et al. 2016; Gehrels et al. 2016; Artale et al. 2020b).

A question arises as to how to weight the galaxies in such schemes, most simply by making use of their absolute luminosities in some pass-band (since that information is more widely available than, for example, more detailed characterization of their star formation histories). With this in mind, in Fig. 12 we plot the ratio of the number of mergers (restricted to $z < 0.05$) occurring per unit luminosity (averaged over all galaxies in the simulation box), as a function of host absolute luminosity, in various pass-bands. A situation in which binary merger rate was exactly proportional to luminosity would result in completely flat curves in this diagram. As can be seen, this is most nearly the case for the g band (both NSNS and eBHNS), which may reflect the balance between an enhanced rate of mergers from relatively young (and therefore bluer) stellar populations and the overall dominance of intermediate and older (redder) populations. In contrast, the (near-IR) H-band magnitude does not provide such a good tracer of merger likelihood, presumably due to large early-type (elliptical/lenticular) galaxies being bright in that band, but producing comparatively few mergers.

5.3 Implications for SGRB host identification

Successfully ejected binaries with long lifespans are likely to merge further away from their hosts due to prolonged migration. The greater their galactocentric radius, the lower the likelihood of a successful association with their parent galaxy, which, as we have seen in previous sections, will bias SGRB redshift samples, for example. It is therefore interesting to ask, if an SGRB detected by *Swift*/BAT is found to be host-less, what can we say about its likely redshift and offset from its parent galaxy, based solely on the peak gamma-ray luminosity?

Fig. 13 shows the distribution of the resulting offsets with redshift for host-less merging systems. Each panel corresponds to a range of peak photon fluxes, Φ, that would be detected by BAT. The colour of each point corresponds to the H-band magnitude of the host galaxy. The majority of events with high photon fluxes $\Phi \gtrsim 100\,\mathrm{cm^{-2}s^{-1}}$ occur between $0.1 \lesssim z \lesssim 0.5$. At all fluxes there are some mergers that are low redshift and have large offsets (>100 arcsec) on the sky from their hosts, making association very challenging. For SGRBs with low photon fluxes ($<1\,\mathrm{ph\,s^{-1}\,cm^{-2}}$; refer to the final panel of Fig. 13) close to the BAT detection threshold, the fraction of these events with faint host galaxies ($H > 26$) is found to be ~ 23, ~ 19, and ~ 38 per cent for BPASS/Bray, BPASS/Hobbs, and COSMIC simulations respectively.

5.4 Impact parameters of SGRBs

In Fig. 14, we compare the impact parameters for an observed sample of 32 SGRBs with well-constrained offsets and redshifts (see Table 5) against our simulated BPASS/Bray SGRB progenitor systems that are detectable by *Swift*/BAT (for the same comparison with BPASS/Hobbs, and COSMIC binaries see figs A8 and B8). The median of the observed SGRB impact parameters is ~ 5.5 kpc. In comparison, for all simulated BAT-detectable SGRBs, we find median impact parameters of 6.1, 11.6, and 4.2 kpc for BPASS/Bray, BPASS/Hobbs, and COSMIC, respectively. When the host-less population of progenitors are excluded, these values are revised to 4.7, 6.2, and 3.8 kpc.

In Table 6, we present the rejection levels for the two-sample Kolmogorov–Smirnov (KS) tests comparing impact parameters for the observed SGRB sample and each binary simulation. We conduct this test for the whole BAT-detectable SGRB samples as well as the sub-samples of afterglow-bright events (see Section 4.2). The most relevant comparison is with the 'with host' samples: COSMIC simulations perform poorly in these tests, due to the typically short life-times and consequently low impact parameters that it produces. Otherwise BPASS/Hobbs matches well, and BPASS/Bray is marginally consistent with the observed sample. The results do not vary significantly if restricted to 'afterglow-bright' systems. Finally, we note that all simulations are reasonably consistent with the < 10 kpc median SGRB galactocentric offset estimated by O'Connor et al. (2020).

6 SUMMARY

Using our new ZELDA code suite along with binary population synthesis codes, specifically BPASS and COSMIC, in addition to the cosmological simulation, EAGLE, we have traced the orbital evolution and host properties of a population of simulated isolated compact binaries from birth to coalescence. We use three binary simulated populations with varied prescriptions which are referred to as, BPASS/Bray, BPASS/Hobbs, and COSMIC. The key differ-

Table 5. Redshift and impact parameter values for the SGRBs used within this study. The E_{iso} is calculated from *Swift*/BAT's 15–350 keV energy band.

GRB	z	IP [kpc]	E_{iso} [$\times 10^{48}$ erg]	Refs.
050509B	0.225	63.40	7.42	[1–5]
050709	0.161	3.64	29.6[a]	[1–4, 6]
050724	0.258	$2.57^{+0.8}_{-0.8}$	83.9	[1–4, 7]
050813	0.719	35.50	219	[1, 3, 8]
051210	>1.400	>24.90	2480	[1, 3]
051221A	0.550	$0.76^{+0.25}_{-0.25}$	2680	[1–4, 9–10]
060502B	0.287	73.30	49.2	[1–4, 11]
060801	1.130	17.60	2290	[1–4, 12–13]
061006	0.436	3.50	1070	[1–3, 14]
061210	0.410	15.60	552	[1–4, 15–17]
070429B	0.902	4.70	460	[1-4, 15, 18–20]
070707	<3.6	–	178 000[a]	[1, 18, 21]
070714B	0.923	3.10	3340	[1–4, 15, 18, 22]
070724A	0.457	$5.46^{+0.14}_{-0.14}$	39.7	[1–4, 15, 18, 23-24]
070729	$0.800^{+0.1}_{-0.1}$	$3.21^{+18.80}_{-18.80}$	897	[3]
070809	0.473	35.40	140	[1–2, 15, 18]
071227	0.381	$15.50^{+0.24}_{-0.24}$	204	[1–3, 14–15, 18]
080503	<4.000	–	16 200	[1, 18]
080905A	0.122	18.50	16.1	[1–4, 18, 25]
090305A	<4.100	–	36 000	[18]
090510	0.903	9.40	4980	[1–3, 15, 18, 26]
100117A	0.915	$1.32^{+0.33}_{-0.33}$	1100	[1–3, 15, 18]
100206A	0.407	$21.90^{+18.10}_{-18.10}$	263	[1–2, 27-28]
100625A	0.452	<19.80	525	[1–2, 27]
100816A	0.804	10.07	7730	[29–30]
101219A	0.718	3.50	3500	[1–2, 27, 31–32]
111117A	2.211	$10.6^{+1.70}_{-1.70}$	19 800	[2, 33–34]
120804A	1.300	$2.20^{+1.20}_{-1.20}$	18 200	[2, 27, 35]
130603B	0.356	$5.21^{+0.17}_{-0.17}$	803	[2, 18, 27, 36–37]
140903A	0.351	$0.5^{+0.2}_{-0.2}$	90.7	[2, 38–40]
150101B	0.134	$7.35^{+0.07}_{-0.07}$	5.84	[2, 41–43]
150424A	0.300	22.50	1080	[2, 44]
160410A	1.717	~0	1590	[45–46]
160624A	0.483	< 11.91	192	[2, 47–48]
160821B	0.162	16.40	13.9	[2, 49–51]
170428A	0.454	$6.90^{+1.70}_{-1.70}$	663	[2, 52]
170817A	0.001	2.13	0.031[a]	[2, 53]
181123B	1.754	$5.08^{+1.38}_{-1.38}$	10 400	[54]
200522A	0.554	$0.93^{+0.19}_{-0.19}$	287	[48, 55]
200826A	0.748	–	13 000[a]	[56]
201221D	1.046	–	6660[a]	[57]

Note. References: [1] Tunnicliffe et al. (2014) [2] Gompertz et al. (2020) [3] Kann et al. (2011) [4] Church et al. (2012) [5] Bloom et al. (2006) [6] Fox et al. (2005) [7] Prochaska et al. (2005) [8] Foley, Bloom & Chen (2005) [9] Berger & Soderberg (2005) [10] Soderberg et al. (2006) [11] Bloom et al. (2007) [12] Cucchiara et al. (2006) [13] Racusin, Burrows & Gehrels (2006) [14] D'Avanzo et al. (2009) [15] Leibler & Berger (2010) [16] Ziaeepour et al. (2006) [17] Berger (2006) [18] Fong & Berger (2013) [19] Perley et al. (2007) [20] Holland, de Pasquale & Markwardt (2007) [21] Piranomonte et al. (2008) [22] Graham et al. (2009) [23] Berger et al. (2009) [24] Kocevski et al. (2010) [25] Rowlinson et al. (2010) [26] Rau, McBreen & Kruehler (2009) [27] Berger (2014) [28] Cenko et al. (2010) [29] Tanvir et al. (2010) [30] Im et al. (2010) [31] Kuin & Gelbord (2011) [32] Chornock & Berger (2011) [33] Selsing et al. (2018) [34] Margutti et al. (2012) [35] Berger et al. (2013) [36] Thone et al. (2013) [37] Levan et al. (2013) [38] Levan et al. (2014) [39] Cucchiara et al. (2014) [40] Troja et al. (2016) [41] Levan et al. (2015) [42] Fong et al. (2015b) [43] Fong et al. (2016) [44] Castro-Tirado et al. (2015) [45] Selsing et al. (2016) [46] Selsing et al. (2019) [47] Cucchiara & Levan (2016) [48] O'Connor et al. (2021) [49] Lamb et al. (2019b) [50] Troja et al. (2019b) [51] Acciari et al. (2021) [52] Izzo et al. (2017) [53] Abbott et al. (2017c) [54] Paterson et al. (2020) [55] Fong et al. (2021) [56] Rothberg et al. (2020) [57] de Ugarte Postigo et al. (2020).
[a]Calculated using *Fermi*/GBM's 10–10 000 keV energy band.

Table 6. Two sample Kolmogorov–Smirnov test rejection levels for the simulated BAT-detectable SGRB progenitors impact parameters as compared against observed SGRBs. The second half of data includes the KS-test rejection levels for the subset of systems that merge in afterglow-bright environments, refer to Section 4.2.

BAT-Detectable SGRBs	Kolmogorov–Smirnov test rejection (per cent)		
	BPASS/Bray	BPASS/Hobbs	COSMIC
All	18	95	81
With Host only	92	64	98
	Afterglow bright events		
All	90	42	98
With Host only	95	79	99

ence between the samples is the employed natal-kick prescriptions and merger time distributions. Most seeded BPASS/Bray binaries merge on relatively long time-scales of 1–10 Gyr with the majority of natal-kick velocities ranging between ~ 100 and 300 km s^{-1}; BPASS/Hobbs systems exhibit a broader range of lifespans with higher kick velocities, with the modal velocity at $v \sim 350$ km s^{-1}; COSMIC systems merge with comparatively short lifespans, < 100 Myr and natal-kick velocities that are typically < 100 km s^{-1}. Despite these differences, we find some conclusions are common to all the models, specifically:

(i) For NSNS and eBHNS SGRB progenitors at merger, we find ~ 50–70 per cent of the hosts to be late-type galaxies, at all redshifts. For COSMIC binaries, the upper limit on this demographics estimate can extend to ~ 80 per cent.

(ii) A consequence of this is that, for low redshift events $z < 0.05$ (i.e. within the current range of GW detection), we find the majority of mergers to arise from relatively blue, star-forming hosts. Thus, we find the g band to be best suited for predicting compact binary merger rates in low redshift galaxies, and hence useful for weighting/prioritizing galaxies for gravitational wave electromagnetic follow-up observations.

(iii) The modal average of the radial offset from the centre of the host galaxy at the time of merger is $\lesssim 10$ kpc. For each binary population used, these values range between ~ 5 and 10 kpc for BPASS/Hobbs systems and eBHNS mergers from the BPASS/Bray sample. For BPASS/Bray NSNS and COSMIC systems, this range varies between ~ 2.5 and 5 kpc. Long-lived systems with $\tau_{merge} \gtrsim 1$ Gyr can potentially travel well beyond 100 kpc from their host galaxy provided that they have natal-kick velocities that are sufficient for them to escape the gravitational potential of their host galaxy.

To gauge the consistency of the zELDA processed binaries and their hosts we compare against the population of well-localized short-duration gamma-ray bursts (SGRBs) (i.e. events with convincing host galaxies and offsets). We achieve this by simulating *Swift*/BAT observations of NSNS and eBHNS mergers from our study, using an assumed luminosity function consistent with literature estimates.

Observationally, some SGRBs have been found to be 'host-less', in the sense that there is no clear association with a galaxy, presumably due to either large offsets at merger and/or because the host is very faint. GRBs without a confident host association will typically have no redshift and impact parameter estimates, biases of these cases must be considered in our comparison. To mimic this, we define simulated binaries to be 'host-less' if either the parent galaxy has a greater than 5 per cent probability of being simply a chance alignment based on the impact parameter (i.e. projected radial offset from galaxy centre) and apparent magnitude of the galaxy, and/or has a host galaxy

with a *H*-band magnitude of $H > 26$ (i.e. requiring deep follow-up observations, e.g. with *HST* to detect). Our findings are:

(i) For both the BPASS/Bray and COSMIC simulations, we find the hosts of the simulated SGRBs to be ~50–60 per cent late-type, and ~15–20 per cent host-less, in reasonable agreement with the demographic distribution of observed hosts (Fong et al. 2013). In contrast, the BPASS/Hobbs sample predicts a much higher proportion of host-less events (~35 per cent), due largely to the typically higher kick velocities, which is likely in excess of the host-less fraction observed.

(ii) The impact parameter distribution of the simulated BAT-detectable SGRBs for BPASS/Bray and BPASS/Hobbs are reasonably consistent with the observed SGRB offsets. In this comparison, however, the COSMIC simulation underpredicts the offsets that are observed, which is a consequence of the lower kick velocities and shorter lifetimes.

It is interesting to ask the question, if an SGRB is found to be host-less, can our simulations give a prior expectation for its most likely redshift, host and projected offset?

(i) For the brightest host-less simulated SGRBs (those with peak fluxes $>10^2$ photons cm^{-2} s^{-1}), the parent galaxies are found to be always at redshifts $z < 1$ and offsets are typically tens of arcsec, but can range up to in excess of ~10^3 arcsec (as expected, the BPASS/Hobbs simulation typically results in rather larger offsets).

(ii) At the other extreme, for bursts close to the *Swift*/BAT detection threshold, we find that the majority of events (for all simulations) to be $z < 1$, but with a significant tail to higher redshifts. Notably, for these faint bursts, a sizable fraction of events (~ 23, ~ 19, and ~ 38 per cent for BPASS/Bray, BPASS/Hobbs, and COSMIC populations, respectively) are found to be host-less by virtue of their hosts being faint ($H > 26$) rather than having large impact parameters.

As a final step, we also considered an additional selection effect, namely that bursts arising in a low ambient density medium (defined here as $n < 10^{-4}$ cm^{-3}) are expected to have on average fainter afterglows, and so would be selected against in observed samples that rely on detection of X-ray or optical counterparts for precise localization.

(i) We estimate the fraction of BAT-detectable SGRBs arising from such low density environments. For the BPASS/Bray, BPASS/Hobbs, and COSMIC samples these fractions are found to be ~ 24, ~ 35, and ~ 13 per cent, respectively.

Overall, we conclude that of the three population synthesis models considered, BPASS/Bray gives results most closely aligning with the available observational constraints i.e. host demographics, and impact parameter distributions. This may be expected as it includes the most sophisticated binary evolution modelling, although this conclusion reflects most strongly the differences in kick velocity than merger time distributions.

Our study does not include binaries that are formed through dynamical processes, for example in globular or open clusters. In comparison to isolated systems, the merger rate of dynamically formed binaries has generally been estimated to be significantly lower. As such, isolated EM-bright compact binaries are expected to be the dominant channel for producing the observed population of SGRBs. If these systems are found to be more common, for instance due to their formation in young stellar clusters, then it will be important to account for their contribution. With further host associations of SGRBs and/or with gravitational waves produced by NSNS and BHNS compact binary mergers, we will be able to further refine and improve constraints on the demographic and offset estimates derived and discussed in this work. Similarly, with a greater sample of observed SGRBs, predictions for the physical input parameters such as the total net-kick velocity and merger time distributions can be tested from the comparison with associated impact parameters.

DATA AVAILABILITY

The cosmological simulation data underlying this article are available at EAGLE[10], for the galaxies used. The BPASS/Bray and BPASS/Hobbs data sets are derived using the BPASS models from BPASS 2.1[11]. The COSMIC binaries used are produced using the COSMIC PYTHON package available at the COSMIC Homepage[12].

REFERENCES

Abbott B. P. et al., 2016, Phys. Rev. Lett., 116, 061102
Abbott B. P. et al., 2017a, Nature, 551, 85
Abbott B. P. et al., 2017b, ApJ, 848, L12
Abbott B. P. et al., 2017c, ApJ, 848, L13
Abbott B. P. et al., 2018, Liv. Rev. Relat., 21, 3
Abbott R. et al., 2021a, Phys. Rev. X, 11, 021053
Abbott R. et al., 2021b, ApJ, 915, L5
Acciari V. A. et al., 2021, ApJ, 908, 90
Ackley K. et al., 2020, A&A, 643, A113
Alexander K. D. et al., 2017, ApJ, 848, L21
Amaro-Seoane P., Miller M. C., Kennedy G. F., 2012, MNRAS, 425, 2401
Andreoni I. et al., 2020, ApJ, 890, 131
Andrews J. J., Mandel I., 2019, ApJ, 880, L8
Arcavi I. et al., 2017, ApJ, 848, L33
Artale M. C., Mapelli M., Giacobbo N., Sabha N. B., Spera M., Santoliquido F., Bressan A., 2019, MNRAS, 487, 1675

[10]http://icc.dur.ac.uk/Eagle/database.php
[11]https://bpass.auckland.ac.nz/
[12]https://cosmic-popsynth.github.io/

Artale M. C., Mapelli M., Bouffanais Y., Giacobbo N., Pasquato M., Spera M., 2020a, MNRAS, 491, 3419

Artale M. C., Bouffanais Y., Mapelli M., Giacobbo N., Sabha N. B., Santoliquido F., Pasquato M., Spera M., 2020b, MNRAS, 495, 1841

Astropy Collaboration, 2013, A&A, 558, A33

Band D. et al., 1993, ApJ, 413, 281

Barbieri C., Salafia O. S., Perego A., Colpi M., Ghirlanda G., 2019, A&A, 625, A152

Belczyński K., Bulik T., 1999, A&A, 346, 91

Belczynski K., Perna R., Bulik T., Kalogera V., Ivanova N., Lamb D. Q., 2006, ApJ, 648, 1110

Belczynski K. et al., 2018, A&A, 615, A91

Berger E., 2006, GRB Coordinates Network, 5965, 1

Berger E., 2009, ApJ, 690, 231

Berger E., 2010, ApJ, 722, 1946

Berger E., 2014, ARA&A, 52, 43

Berger E., Soderberg A. M., 2005, GRB Coordinates Network, 4384, 1

Berger E., Cenko S. B., Fox D. B., Cucchiara A., 2009, ApJ, 704, 877

Berger E. et al., 2013, ApJ, 765, 121

Bloom J. S., Sigurdsson S., Pols O. R., 1999, MNRAS, 305, 763

Bloom J. S., Kulkarni S. R., Djorgovski S. G., 2002, AJ, 123, 1111

Bloom J. S. et al., 2006, ApJ, 638, 354

Bloom J. S. et al., 2007, ApJ, 654, 878

Bovy J., 2015, ApJS, 216, 29

Branchesi M., 2016, J. Phys. Conf. Ser., 718, 022004

Bray J. C., Eldridge J. J., 2016, MNRAS, 461, 3747

Bray J. C., Eldridge J. J., 2018, MNRAS, 480, 5657

Breivik K. et al., 2020, ApJ, 898, 71

Bromberg O., Nakar E., Piran T., Sari R., 2013, ApJ, 764, 179

Bulik T., Belczyński K., Zbijewski W., 1999, MNRAS, 309, 629

Bullock J. S., Kolatt T. S., Sigad Y., Somerville R. S., Kravtsov A. V., Klypin A. A., Primack J. R., Dekel A., 2001, MNRAS, 321, 559

Calvi R., Vulcani B., Poggianti B. M., Moretti A., Fritz J., Fasano G., 2018, MNRAS, 481, 3456

Carlberg R. G. et al., 1997, ApJ, 485, L13

Castro-Tirado A. J., Sanchez-Ramirez R., Lombardi G., Rivero M. A., 2015, GRB Coordinates Network, 17758, 1

Cenko S. B., Bloom J. S., Perley D. A., Cobb B. E., Morgan A. N., Miller A. A., Modjaz M., James B., 2010, GRB Coordinates Network, 10389, 1

Choksi N., Volonteri M., Colpi M., Gnedin O. Y., Li H., 2019, ApJ, 873, 100

Chornock R., Berger E., 2011, GRB Coordinates Network, 11518, 1

Chornock R. et al., 2017, ApJ, 848, L19

Chruslinska M., Nelemans G., Belczynski K., 2019, MNRAS, 482, 5012

Church R. P., Levan A. J., Davies M. B., Tanvir N., 2011, MNRAS, 413, 2004

Church R. P., Levan A. J., Davies M. B., Tanvir N., 2012, Mem. Soc. Astron. Ital. Suppl., 21, 104

Comerford J. M., Natarajan P., 2007, MNRAS, 379, 190

Correa C. A., Schaye J., Clauwens B., Bower R. G., Crain R. A., Schaller M., Theuns T., Thob A. C. R., 2017, MNRAS, 472, L45

Corsi A. et al., 2018, ApJ, 861, L10

Coulter D. A. et al., 2017, Science, 358, 1556

Cowperthwaite P. S. et al., 2017, ApJ, 848, L17

Crain R. A. et al., 2015, MNRAS, 450, 1937

Cucchiara A., Levan A. J., 2016, GRB Coordinates Network, 19565, 1

Cucchiara A., Fox D., Berger E. P. A. P., 2006, GRB Coordinates Network, 5470, 1

Cucchiara A., Cenko S. B., Perley D. A., Capone J., Toy V., 2014, GRB Coordinates Network, 16774, 1

D'Avanzo P. et al., 2009, A&A, 498, 711

de Ugarte Postigo A., Kann D. A., Izzo L., Thoene C. C., Blazek M., Agui Fernandez J. F., Lombardi G., 2020, GRB Coordinates Network, 29132, 1

Dichiara S., Troja E., O'Connor B., Marshall F. E., Beniamini P., Cannizzo J. K., Lien A. Y., Sakamoto T., 2020, MNRAS, 492, 5011

Eldridge J. J., Stanway E. R., Xiao L., McClelland L. A. S., Taylor G., Ng M., Greis S. M. L., Bray J. C., 2017, PASA, 34, e058

Evans P. A. et al., 2016, MNRAS, 455, 1522

Evans P. A. et al., 2017, Science, 358, 1565

Fang T., Bullock J., Boylan-Kolchin M., 2013, ApJ, 762, 20

Fernández J. J., Kobayashi S., 2019, MNRAS, 487, 1200

Foley R. J., Bloom J. S., Chen H. W., 2005, GRB Coordinates Network, 3808, 1

Fong W., Berger E., 2013, ApJ, 776, 18

Fong W. et al., 2013, ApJ, 769, 56

Fong W., Berger E., Margutti R., Zauderer B. A., 2015a, ApJ, 815, 102

Fong W., Berger E., Fox D., Shappee B. J., 2015b, GRB Coordinates Network, 17333, 1

Fong W. et al., 2016, ApJ, 833, 151

Fong W. et al., 2017, ApJ, 848, L23

Fong W. et al., 2021, ApJ, 906, 127

Foucart F., Duez M. D., Kidder L. E., Nissanke S. M., Pfeiffer H. P., Scheel M. A., 2019, Phys. Rev. D, 99, 103025

Fox D. B. et al., 2005, Nature, 437, 845

Fragione G., Kocsis B., 2018, Phys. Rev. Lett., 121, 161103

Fragos T., Willems B., Kalogera V., Ivanova N., Rockefeller G., Fryer C. L., Young P. A., 2009, ApJ, 697, 1057

Frith W. J., Metcalfe N., Shanks T., 2006, MNRAS, 371, 1601

Fryer C. L., Belczynski K., Wiktorowicz G., Dominik M., Kalogera V., Holz D. E., 2012, ApJ, 749, 91

Furlong M. et al., 2015, MNRAS, 450, 4486

Gehrels N. et al., 2005, Nature, 437, 851

Gehrels N., Cannizzo J. K., Kanner J., Kasliwal M. M., Nissanke S., Singer L. P., 2016, ApJ, 820, 136

Ghirlanda G. et al., 2016, A&A, 594, A84

Giacobbo N., Mapelli M., 2018, MNRAS, 480, 2011

Gompertz B. P. et al., 2018, ApJ, 860, 62

Gompertz B. P., Levan A. J., Tanvir N. R., 2020, ApJ, 895, 58

Graham J. F. et al., 2009, ApJ, 698, 1620

Haggard D., Nynka M., Ruan J. J., Kalogera V., Cenko S. B., Evans P., Kennea J. A., 2017, ApJ, 848, L25

Hajela A. et al., 2019, ApJ, 886, L17

Hallinan G. et al., 2017, Science, 358, 1579

Hayashi K., Kawaguchi K., Kiuchi K., Kyutoku K., Shibata M., 2021, Phys. Rev. D., 103, 043007

Hinderer T. et al., 2019, Phys. Rev. D, 100, 063021

Hjorth J. et al., 2005, ApJ, 630, L117

Hobbs G., Lorimer D. R., Lyne A. G., Kramer M., 2005, MNRAS, 360, 974

Holland S. T., de Pasquale M., Markwardt C. B., 2007, GRB Coordinates Network, 7145, 1

Huerta E. A. et al., 2019, Nat. Rev. Phys., 1, 600

Hunter J. D., 2007, Comput. Sci. Eng., 9, 90

Hurley J. R., Tout C. A., Pols O. R., 2002, MNRAS, 329, 897

Im M., Park W. K., Pak S., Jeong H., Kim E., Kim J., 2010, GRB Coordinates Network, 11108, 1

Im M. et al., 2017, ApJ, 849, L16

Izzo L., Cano Z., de Ugarte Postig A., Kann D. A., Thoene C., Geier S., 2017, GRB Coordinates Network, 21059, 1

Jiang Z. et al., 2020, MNRAS, 498, 926

Jin Z.-P. et al., 2016, Nat. Commun., 7, 12898

Jin Z.-P., Covino S., Liao N.-H., Li X., D'Avanzo P., Fan Y.-Z., Wei D.-M., 2020, Nat. Astron., 4, 77

Kann D. A. et al., 2011, ApJ, 734, 96

Kasliwal M. M. et al., 2017, Science, 358, 1559

Katz J. I., Canel L. M., 1996, ApJ, 471, 915

Kawaguchi K., Kyutoku K., Shibata M., Tanaka M., 2016, ApJ, 825, 52

Kocevski D. et al., 2010, MNRAS, 404, 963

Kouveliotou C., Meegan C. A., Fishman G. J., Bhat N. P., Briggs M. S., Koshut T. M., Paciesas W. S., Pendleton G. N., 1993, ApJ, 413, L101

Kroupa P., 2001, MNRAS, 322, 231

Kuin N. P. M., Gelbord J. M., 2011, GRB Coordinates Network, 11575, 1

Lamb G. P. et al., 2019a, ApJ, 870, L15

Lamb G. P. et al., 2019b, ApJ, 883, 48

Lee W. H., Ramirez-Ruiz E., 2007, New J. Phys., 9, 17

Leibler C. N., Berger E., 2010, ApJ, 725, 1202

Levan A. J. et al., 2006, ApJ, 648, L9

Levan A. J. et al., 2007, MNRAS, 378, 1439

Levan A. J., Tanvir N. R., Wiersema K., Hartoog O., Kolle K., Mendez J., Kupfer T., 2013, GRB Coordinates Network, 14742, 1

Levan A. J., Cenko S. B., Cucchiara A., Perley D. A., 2014, GRB Coordinates Network, 16784, 1

Levan A. J., Hjorth J., Wiersema K., Tanvir N. R., 2015, GRB Coordinates Network, 17281, 1

Levan A. J. et al., 2017, ApJ, 848, L28

Licquia T. C., Newman J. A., 2015, ApJ, 806, 96

Lien A. et al., 2016, ApJ, 829, 7

Lyman J. D. et al., 2018, Nat. Astron., 2, 751

Madau P., Dickinson M., 2014, ARA&A, 52, 415

Mainetti D., Lupi A., Campana S., Colpi M., 2016, MNRAS, 457, 2516

Maller A. H., Bullock J. S., 2004, MNRAS, 355, 694

Mandhai S., Tanvir N., Lamb G., Levan A., Tsang D., 2018, Galaxies, 6, 130

Mapelli M., Giacobbo N., Toffano M., Ripamonti E., Bressan A., Spera M., Branchesi M., 2018, MNRAS, 481, 5324

Margutti R. et al., 2012, ApJ, 756, 63

Margutti R. et al., 2017, ApJ, 848, L20

Mazets E. P., Golenetskii S. V., 1981, Ap&SS, 75, 47

McAlpine S. et al., 2016, Astron. Comput., 15, 72

McCarthy K. S., Zheng Z., Ramirez-Ruiz E., 2020, MNRAS, 499, 5220

McCully C. et al., 2017, ApJ, 848, L32

McKinney W., 2010, in van der Walt S., Millman J., eds, Proceedings of the 9th Python in Science Conference, Austin, TX, p. 51

Mészáros P., Rees M. J., 1997, ApJ, 476, 232

Mészáros P., Fox D. B., Hanna C., Murase K., 2019, Nat. Rev. Phys., 1, 585

Metcalfe N., Shanks T., Weilbacher P. M., McCracken H. J., Fong R., Thompson D., 2006, MNRAS, 370, 1257

Miyamoto M., Nagai R., 1975, PASJ, 27, 533

Mogushi K., Cavaglià M., Siellez K., 2019, ApJ, 880, 55

Mooley K. P. et al., 2018, Nature, 561, 355

Morgan R. et al., 2020, ApJ, 901, 83

Murase K., Bartos I., 2019, Ann. Rev. Nucl. Part. Sci., 69, 477

Nakar E., 2007, Phys. Rep., 442, 166

Narayan R., Paczynski B., Piran T., 1992, ApJ, 395, L83

Narayan R., Piran T., Kumar P., 2001, ApJ, 557, 949

Navarro J. F., Frenk C. S., White S. D. M., 1996, ApJ, 462, 563

Nicholl M. et al., 2017, ApJ, 848, L18

Nynka M., Ruan J. J., Haggard D., Evans P. A., 2018, ApJ, 862, L19

O'Connor B., Beniamini P., Kouveliotou C., 2020, MNRAS, 495, 4782

O'Connor B. et al., 2021, MNRAS, 502, 1279

Oliphant T. E., 2006, A Guide to NumPy, Vol. 1. Trelgol Publishing, USA

Palmese A. et al., 2017, ApJ, 849, L34

Paterson K. et al., 2020, ApJ, 898, L32

Paul D., 2018, MNRAS, 477, 4275

Perego A., Radice D., Bernuzzi S., 2017, ApJ, 850, L37

Perley D. A., Bloom J. S., Modjaz M., Poznanski D., Thoene C. C., 2007, GRB Coordinates Network, 7140, 1

Perna R., Belczynski K., 2002, ApJ, 570, 252

Pian E. et al., 2017, Nature, 551, 67

Piranomonte S. et al., 2008, A&A, 491, 183

Piro L. et al., 2019, MNRAS, 483, 1912

Planck Collaboration XVI, 2014, A&A, 571, A16

Price-Whelan A. M. et al., 2018, AJ, 156, 123

Prochaska J. X., Bloom J. S., Chen H. W., Hansen B., Kalirai J., Rich M., Richer H., 2005, GRB Coordinates Network, 3700, 1

Qu Y. et al., 2017, MNRAS, 464, 1659

Racusin J. L., Burrows D. N., Gehrels N., 2006, GRB Coordinates Network, 5773, 1

Rau A., McBreen S., Kruehler T., 2009, GRB Coordinates Network, 9353, 1

Resmi L. et al., 2018, ApJ, 867, 57

Rodriguez C. L., Loeb A., 2018, ApJ, 866, L5

Rodriguez C. L., Morscher M., Pattabiraman B., Chatterjee S., Haster C.-J., Rasio F. A., 2015, Phys. Rev. Lett., 115, 051101

Rodriguez C. L., Chatterjee S., Rasio F. A., 2016, Phys. Rev. D, 93, 084029

Rothberg B., Kuhn O., Veillet C., Allanson S., 2020, GRB Coordinates Network, 28319, 1

Rowlinson A. et al., 2010, MNRAS, 408, 383

Ruiz M., Paschalidis V., Tsokaros A., Shapiro S. L., 2020, Phys. Rev. D, 102, 124077

Samsing J., D'Orazio D. J., 2018, MNRAS, 481, 5445

Santoliquido F., Mapelli M., Bouffanais Y., Giacobbo N., Di Carlo U. N., Rastello S., Artale M. C., Ballone A., 2020, ApJ, 898, 152

Sari R., Piran T., Narayan R., 1998, ApJ, 497, L17

Schaye J. et al., 2015, MNRAS, 446, 521

Selsing J. et al., 2016, GRB Coordinates Network, 19274, 1

Selsing J. et al., 2018, A&A, 616, A48

Selsing J. et al., 2019, A&A, 623, A92

Shappee B. J. et al., 2017, Science, 358, 1574

Shen S., Cooke R. J., Ramirez-Ruiz E., Madau P., Mayer L., Guedes J., 2015, ApJ, 807, 115

Shibata M., Taniguchi K., 2011, Liv. Rev. Relat., 14, 6

Smartt S. J. et al., 2017, Nature, 551, 75

Soares-Santos M. et al., 2017, ApJ, 848, L16

Soderberg A. M. et al., 2006, ApJ, 650, 261

Stanway E. R., Eldridge J. J., 2018, MNRAS, 479, 75

Sun H., Zhang B., Li Z., 2015, ApJ, 812, 33

Tanaka M., Hotokezaka K., Kyutoku K., Wanajo S., Kiuchi K., Sekiguchi Y., Shibata M., 2014, ApJ, 780, 31

Tanaka M. et al., 2017, PASJ, 69, 102

Tan W.-W., Yu Y.-W., 2020, ApJ, 902, 83

Tanvir N. R. et al., 2010, GRB Coordinates Network, 11123, 1

Tanvir N. R., Levan A. J., Fruchter A. S., Hjorth J., Hounsell R. A., Wiersema K., Tunnicliffe R. L., 2013, Nature, 500, 547

Tanvir N. R. et al., 2017, ApJ, 848, L27

Thob A. C. R. et al., 2019, MNRAS, 485, 972

Thone C. C., de Ugarte Postigo A., Gorosabel J., Tanvir N., Fynbo J. P. U., 2013, GRB Coordinates Network, 14744, 1

Troja E. et al., 2016, ApJ, 827, 102

Troja E. et al., 2017, Nature, 551, 71

Troja E. et al., 2019a, MNRAS, 489, 1919

Troja E. et al., 2019b, MNRAS, 489, 2104

Troja E. et al., 2020, MNRAS, 498, 5643

Tsutsui R., Yonetoku D., Nakamura T., Takahashi K., Morihara Y., 2013, MNRAS, 431, 1398

Tunnicliffe R. L. et al., 2014, MNRAS, 437, 1495

van de Voort F., Pakmor R., Grand R. J. J., Springel V., Gómez F. A., Marinacci F., 2020, MNRAS, 494, 4867

Villar V. A. et al., 2017, ApJ, 851, L21

Virtanen P. et al., 2020, Nat. Methods, 17, 261

Wanderman D., Piran T., 2015, MNRAS, 448, 3026

Wang H. et al., 2017, ApJ, 851, L18

Ye C. S., Fong W.-f., Kremer K., Rodriguez C. L., Chatterjee S., Fragione G., Rasio F. A., 2020, ApJ, 888, L10

Yonetoku D., Nakamura T., Sawano T., Takahashi K., Toyanago A., 2014, ApJ, 789, 65

Zevin M., Kelley L. Z., Nugent A., Fong W.-f., Berry C. P. L., Kalogera V., 2020, ApJ, 904, 190

Zhang B., Fan Y. Z., Dyks J., Kobayashi S., Mészáros P., Burrows D. N., Nousek J. A., Gehrels N., 2006, ApJ, 642, 354

Zhang B. et al., 2007, ApJ, 655, 989

Ziaeepour H. et al., 2006, GRB Coordinates Network, 5948, 1

SUPPORTING INFORMATION

Supplementary data are available at *MNRAS* online.

Appendix A. BPASS/Hobbs Binaries.
Appendix B. COSMIC Binaries.

Please note: Oxford University Press is not responsible for the content or functionality of any supporting materials supplied by the authors. Any queries (other than missing material) should be directed to the corresponding author for the article.

This paper has been typeset from a TeX/LaTeX file prepared by the author.